The synthesised powders were characterised for crystalline phases by powder X-ray diffraction (XRD) (using D8 Advance, Bruker, Cu *K*α, Ni filter, λ=1.540598 Å, 40 kV, 30 mA). A field-emission scanning electron microscope equipped with energy-dispersive X-ray spectrometer (JSM-6335F, JEOL) was used in the examination of particle shape and size and elemental composition. In order to evaluate the aggregation, size distributions of the bulk powder samples were measured by light scattering technique (using Zetasizer Nano S, Malvern Instruments, 4 mW He-Ne laser operated at 633 nm, particle size range 0.3nm-10μm).

RESULTS & DISCUSSION

Although different lead precursors were used in the study, every reaction apparently provided the same off-white powders mixed with some red-block crystals, which were identified as lead oxide by XRD study. Although the contamination of lead oxide in the prepared powders seemed to be inevitable, they could be simply removed by washing with dilute acetic acid solution [12]. After the acid washing, it was found that only $Pb(NO_3)_2$ gave the well crystallised PZ while poorly crystallised powders were obtained from the other lead precursors as depicted in Fig. 55. This could be attributed to the low solubility of these lead precursors in aqueous solution compared to the readily dissolved $Pb(NO_3)_2$ 13]. The hardly dissolved lead precursors might bring about an insufficient nutrient in the solution and consequently the nucleation and crystal growth could not occur properly.

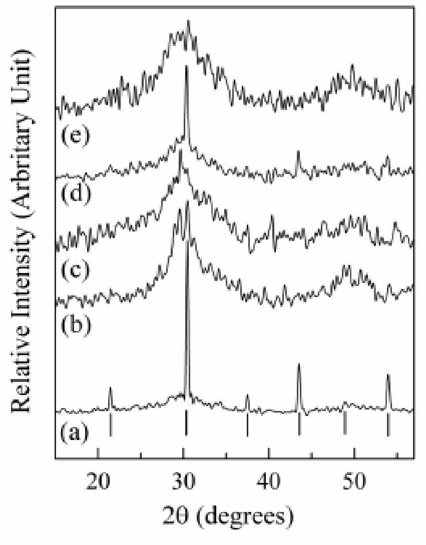

Fig. 55 *XRD patterns of the powders obtained from reactions between $ZrO(NO_3)_2.H_2O$ and different lead precursors in 14 mole dm^{-3} KOH solution for 3 h: (a) $Pb(NO_3)_2$, (b) $Pb(CH_3COO)_2$, (c) PbF_2, (d) $PbCl_2$ and (e) PbI_2. The vertical bars indicate diffraction characteristics of PZ (ICSD 077-0856).*

For the $Pb(NO_3)_2$ case, according to the XRD patterns of the acid-treated powders as shown in Fig. 56, a very high KOH concentration of 14 mole dm^{-3} was required for the success of the synthesis. Lower concentrations resulted in poorly crystallised powders. However, a development in intensity of the *(200)* diffraction peak with increasing KOH concentration was apparent, suggesting the evolvement of the desired PZ. Another observation was a substantial reduction of the effective reaction time from days to hours when compared with the conventional hydrothermal synthesis [8].

According to former studies on similar issues, the observed phenomena could be explained as follows. Under commonly used hydrothermal conditions, the formation of nanocrystalline ZrO_2 as the hydrolysis product of aqueous $ZrO(NO_3)_2$ [14] could also be accelerated by microwave heating. This caused the breaking of large water clusters in the hydration sphere and the formation of the smaller ones [15]. Such mechanism increased the mobility of the dissolved lead species as well as the number of reaction sites on the occurring ZrO_2 surfaces for the hydrated lead ion-water clusters to react. A rapid synthesis should therefore be expected. According to the same studies, the hydrolysis of the aqueous $ZrO(NO_3)_2$ also resulted in the generation of nitric acid, which could neutralise the hydroxide species in solution [14]. In addition, there was evidence for the reduced electrolytic reaction of the KOH solution by the microwave radiation [16]. These phenomena were probably responsible for the increase in the high KOH concentration required in this study. This assumption was supported by the experiment in which a higher microwave power of 810 W was used. Rather than the desired PZ, mixtures of different oxides of lead and zirconium were obtained, which are the expected products of the hydrolysis reactions of the metal salts.

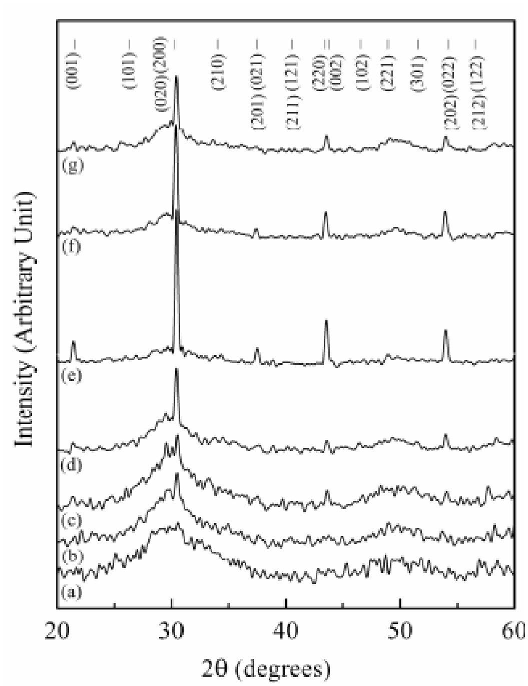

Fig. 56 *XRD patterns of the powders obtained from the reaction between* $ZrO(NO_3)_2.H_2O$ *and* $Pb(NO_3)_2$ *at 720 W for 3 h in different concentrations of KOH solution: (a) 6 (b) 8 (c) 10 (d) 12 and (e) 14 mole* dm^{-3}*, compared to those obtained in 14 mole* dm^{-3} *KOH solution with different reaction times: (f) 4 hours and (g) 5 h. The reference pattern is shown with vertical bars (ICSD 077-0856).*

Based on the XRD patterns of the acid-treated powders, the synthesised PZ could be readily indexed as the orthorhombic *Pbma* phase with refined cell parameters a=5.87(1) Å, b=5.88(2) Å and c=4.15(2) Å (ICSD 077-0856). These results were well consistent with the conventional hydrothermal case, although the refined c parameter was shorter than the conventional heating case, c=4.27(3) Å [8], but closer to the standard, c=4.134 Å (ICSD 077-0856).

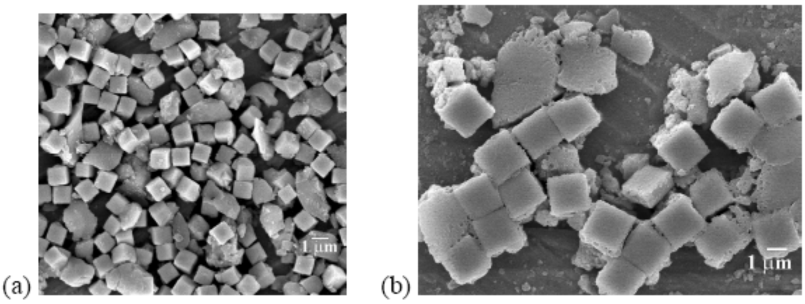

Fig. 57 *Typical FESEM photographs of PZ particles with corresponding XRD patterns shown in Figs. 56(e) and 56(g) for crystals (a) and (b) respectively.*

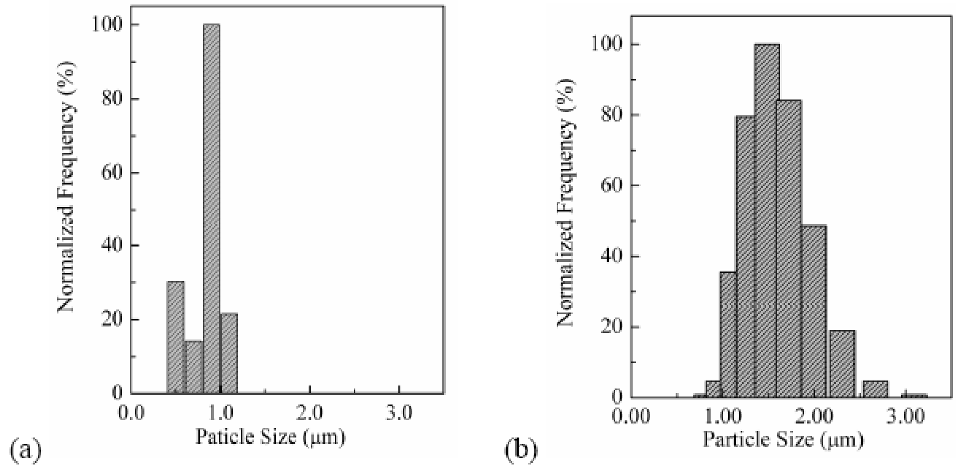

Fig. 58 Particle size distribution of the cubic PZ particles measured from (a) FESEM images and (b) light scattering experiment (measured on the same powder sample).

The field-emmision scanning electron microscopic (FESEM) images, as typically illustrated in Fig. 57(a), showed that the powders largely consisted of discrete cubic particles although some particles with irregular shape were also present. The energy-dispersive X-ray spectroscopic measurements on the surface of several cubic particles indicated stoichiometric Pb:Zr, whereas the irregular-shape particles were found to be Zr-rich. This could account for the noisy background observed for the XRD patterns [Fig. 56(e)]. The sizes of the cubic particles measured from the FESEM images were distributed in a significantly narrow range of 0.4-1.2 μm with approximately 60% of the population having a size of about 1 μm [Fig. 58(a)]. Light scattering experiment on the bulk powder samples showed slightly larger particle sizes distributed mostly between 1-2 μm [Fig. 58(b)]. The difference in particle sizes obtained from the two techniques should be due to a potentially biased analysis of the data. The non-spherical morphology of the particles normally introduces statistical errors to the laser light scattering data while a tendency of the particles to rest with preferred orientation on stub can induce bias in the data representation of the FESEM [17].

Thus, in comparison to the PZ powders derived from a conventional hydrothermal reaction where the particles were reportedly distributed in a 5-15 μm range with an average diameter of 7.5 μm [8], the pronouncedly narrower size distribution and the substantially smaller PZ particles have been achieved, although the negative effect on phase purity of the synthesised PZ and the contamination of some irregular Zr-rich particles were observed. A large number of nucleation induced by the localised microwave heating and the mechanism as described above, coupled with a poor crystal growth due to instantaneous and rapid ramping of such heating, could be the reasons for the approximate uniformity in the particle size [18-19]. Considering the PZ powders obtained from other chemical routes such as precipitation [20] and microemulsion [21], the apparent uniformity in particle shape and size may not be new. Both of these techniques can also give PZ powders composing of mono-dispersed spherical particles typically 20 nm in diameter. However, calcination is required by both techniques, resulting in an unavoidable high temperature treatment and disadvantages incurred therein. As for the modified solid-state preparation of PZ powders, the problems with aggregation and particles with irregular shapes cannot be surmounted even though the vibro-milling is applied for over 25 h [22].

The extension of the microwave heating time from 3 h to 5 h resulted in a reduction in intensity of the most intense *(200)* diffraction peak of the orthorhombic PZ and the appearing of a broad lump at the base of this peak as shown in Fig. 56 (e-g). The FESEM images [Fig. 57(b)] showed that the particles remained in the same cubic shape, although the bubbled surfaces and the necking between the adjacent particles could be observed. This indicated the boiling on the surfaces of these cubic PZ particles, which could be the result of a heat accumulation. The enlargement of the particles, which is a reflection of the particle growth process, and the disappearing of irregular particles with extended reaction time were also apparent.

CONCLUSIONS

In order to promote the mono-dispersion and the uniformity in shape and size of the hydrothermally derived PZ particles without the assistance of organic additives, microwave heating was attempted. The occurrence of lead oxide seemed to be inevitable and washing with dilute acetic acid was necessary. Among different variables studied, the type of lead precursor and the KOH concentration were most critical in the success of the synthesis. It was shown that the critical KOH concentration and the optimal microwave heating time were 14 mole dm^{-3} and 3 h respectively. The highly dispersed cubic lead zirconate particles of approximately 1 μm in size could be synthesised in only 3 h at 720 W of microwave heating. In comparison to conventional hydrothermal synthesis, the merits of the microwave method were clearly reflected by a shortening in hydrothermal reaction time, a reduction in particle size, an improved particle mono-dispersion, and a uniform particle size. However, the negative effects on the purity of synthesised powders, viz. the contamination of irregular particles, and the requirement for a very high concentration of potassium hydroxide mineraliser should be noted.

REFERENCES

1. T. Asada and Y. Koyama, *Phys. Rev. B* **75** (2007) 214111-214121.
2. C.Z. Rosen, B.V. Hiremath and R.E. Newnham, “Key Papers in Physics; Piezoelectricity”, American Institute of Physics, New York, (1992**)** 159-181.
3. K. Yamakawa, S. Trolier-McKinstry and J. P. Dougherty, *Appl. Phys. Lett.* **67** (1995) 2014-2016.
4. P. Ayyub, S. Chattopadhyay, K. Sheshadri and R. Lahiri, “The nature of ferroelectric order in finite systems”, *Nano Mater.*, **1999**, *12*, 713-718.
5. Khamman, W. Chaisan, R. Yimnirun and S. Ananta, *Mater. Lett.* **61** (2007) 2822-2826.
6. E.D. Ion, B. Malic and M. Kosec, *J. Eur. Ceram. Soc.* **27** (2007) 4349-4352.
7. E.E. Oren, E. Taspinar and A.C. Tas, *J. Am. Ceram. Soc.* **80** (1997) 2714-2716.
8. A. Rujiwatra, S. Tapala, S. Luachan, O. Khamman and S. Ananta, *Mater. Lett.* **60** (2006) 2893-2895.
9. G. Xu, G. Zhao, Z. Ren, G. Shen and G. Han, *Mater. Lett.* **60** (2006) 685-688.
10. Z. Lu, J. Liu, Y. Tang and W. Li, *Inorg. Chem. Commun.* **7** (2004) 731-733.
11. W.L. Sin, K.H. Wong and P. Li, *Acta Physica. Polonica. A* **111** (2007) 165-171.
12. S. Tapala, N. Thammajak, P. Laorattanakul and A. Rujiwatra, *Mater. Lett.* **62** (2008) 3685-3687.
13. J. G. Speight, “Lange’s Handbook of Chemistry”, 16th Edn., McGraw-Hill, New York (2005).
14. Y.V. Kolen’ko, V.D. Maximov, A.A. Burukhin, V.A. Muhanov and B.R. Churagulov, *Mater. Sci. Eng. C* **23** (2003) 1033-1038.
15. R. Walczak and J. A. Dziuban, *Sens. Actuators A* **116** (2004**)** 161-170.
16. D. R. Stanisavljev, T. D. Grozdić, M. P. Marĉeta Kaninski, A. R. Djordjević and D. Lj. Stojić, *Electrochem. Commun.* **9** (2007) 901-904.
17. A. Jillavenkatesa, S.J. Dapkunas and L.-S.H. Lum, “Particle Size Characterization; Practice Guide”, U.S. Government Printing Office, Washington, D.C., (2001).
18. D.E. Clark and W.H. Sutton, *Annu. Rev. Mater. Sci.* **26** (1996) 299-331.
19. P. Lidström, J. Tierney, B. Wathey and J. Westman, *Tetrahedron* **51** (2001) 9225-9283.
20. T. Ko and D. -K. Hwang, *Mater. Lett.* **57** (2003) 2472-2479.
21. J. Fang, J. Wang, S.-C. Ng, L.-M. Gan, C.H. Quek and C.-H. Chew, *Mater. Lett.* **36** (1998) 179-185.
22. Khamman, W. Chaisan, R. Yimnirun and S. Ananta, *Mater. Lett.* **61** (2007) 2822-2826.

CHAPTER XI

SOLVOTHERMAL SYNTHESIS, SINTERING BEHAVIOR AND DIELECTRIC PROPERTIES OF POTASSIUM NIOBATE FINE POWDERS

Kittichai Jinachai, Athipong Ngamjarurojana, **Apinpus Rujiwatra**

Chiang Mai Journal of Science **38**(2) (2011) 252-262.

INTRODUCTION

The emergence of the "*green attitude*" has resulted in the attempts to develop the green alternatives for various technologically important materials and processes including lead, despise of its important role technologically. Along this line, potassium niobate ($KNbO_3$, KN) has appeared as one of potential candidates for the lead-free piezoelectric materials. This is due to its excellent inherent properties and potential applications, for example, as an optical wave guide and devices for frequency doubling, holographic storage and surface acoustic wave [1-5]. The material is conventionally prepared by solid state reactions, which demand high temperatures and multiple cycles of heating-and- grinding to assure the completeness of the reactions [6]. Besides being the energy consumable process, the other drawbacks of the solid-state processes such as the formation of undesired impurities and aggregations are inherent [7]. During the last decade, the hydrothermal technique has been proved to be efficient for the preparation of KN in various forms, including fine powder, one dimensional structure and thin film [8-11]. Despise of the promising future of the material and the technique, the practical application and commercialization of KN yet faces a major problem with sintering. At effective sintering temperature and duration, the rapid vaporization of potassium oxide (K_2O) and the large difference in properties of the cation involved result in the chemical control and densification problems [1]. The additions of other aiding compounds, such as magnesium oxide (MgO) and lead oxide (PbO), were reported to relieve the problems [12, 13].

Here, the adaptation of hydrothermal process by the use of mixed water-ethyl alcohol as reaction medium for the preparation of KN fine powders is described. The application of the ultrasonic wave on the reaction mixtures in prior to the synthesis is discussed. The sintering behaviour and the preliminary investigation of the dielectric properties of the sintered ceramics are reported.

EXPERIMENTAL

The mixtures of niobium oxide (Nb_2O_5, Sigma-Aldrich 99.99%, 0.0056 mol) and potassium hydroxide (KOH, Merck 85%, 0.0028 mol) were first prepared in mixed water-ethyl alcohol liquid medium (0.278 mol of water, 0.086 mol of ethyl alcohol; C_2H_5OH, Merck 99.9%). The employed amount of KOH functioning as both reagent and mineralizer in the synthesis is the amount reported as the critical limit providing the successful synthesis [14]. Each mixture was then stirred and transferred into Teflon liners up to *ca.* 80% filling volume capacity. The mixtures were subsequently subjected to an autogenous pressure developed at 200 ^{o}C for 1-24 h. In order to study the effect of ultrasonication, some samples are ultrasonicated at 40(±5) ^{o}C for 1 h using a laboratory ultrasonic bath (Bandelin Electronic RK255H, 160/320W, 35kHz) before the reactions. The synthesized powders were finally recovered by filtration and washed with water until the pH of the filtrate was *ca.* 7 to assure the complete removal of the alkali.

Powder X-ray diffraction (XRD; Bruker D8 Advance diffractometer, Ni-filtered, Cu *K*a, λ=1.54098 Å, 40 kV, 30 mA) was used in characterizing the synthesized crystalline phases. Lattice parameters of these phases were refined from the collected XRD patterns. Selected area electron diffraction (SAED) equipped by a transmission electron microscope (TEM; JEOL JEM-2010) was also used in characterizing growth direction of the elongated particles, whereas a field emission scanning electron microscope (SEM; JEOL JSM-6335F) was used in examining morphologies and sizes of the composing particles.

The synthesized powders composing of a single orthorhombic KN according to the XRD results were chosen for the sintering experiments. The powders were ground and pressed uniaxially at 100 bars and room temperatures to make the pellets of 10.15 mm in diameter and 2.45-2.75 mm in thickness. The obtained pellets were then sintered at 1,025 ^{o}C for 1 hour (Carbolite, 2416CG) using a heating-cooling rate of 3 ^{o}C min^{-1}. After the sintering, densities of the sintered ceramics were evaluated using Archimedes technique [15]. Phase and microstructure of the sintered pellets were investigated by XRD and FESEM, respectively.

The dielectric properties of the sintered ceramics were studied as functions of both temperature and frequency using an automated dielectric measurement system and a silver electrode (Dupont, QS 171), which was prepared by printing on the lapped surfaces followed by firing at 600 ^{o}C for 1 h. The computer-controlled dielectric measurement system consists of a precision LCR meter (Thonghui, TH2819A) and a temperature chamber. The temperature dependent measurements were performed using a Keithley Model 2,000-digit multimeter which was equipped by a temperature chamber, when the capacitance and the dielectric loss tangent were determined over the temperature range of 50-500 ^{o}C with the frequency ranging from 0.1 to 100 kHz.

RESULTS & DISCUSSION

Figures 59 and 60 shows the XRD patterns of the powders obtained from the reactions conducted at 200 ^{o}C for varied reaction times, with and without prior ultrasonication for an hour, respectively. The application of the ultrasonication as described did not show any significant difference in the XRD patterns of the synthesized powders. When the reactions were conducted for an hour, the presence of the other diffraction peaks which were not of the desired KN was plain. The identification of these phases could not be precisely done due to a deficiency in number and intensity of these peaks. It can be nonetheless ascertained that the formation of KN, which could be indexed as the orthorhombic phase with space group *Cm2m* (JCPDS 32-822), already occurred as the major phase. According to the XRD results, the pure phase of KN could be obtained after 3 h, irrespective to the application of the prior ultrasonication on the reaction mixtures. The obtained KN powders could be readily indexed and refined in orthorhombic *Cm2m* (JCPDS 32-822), giving a = 5.689(8)-5.695(8), b = 5.721(11)-5.737(10) and c = 3.982(11)-3.984(12)). There was not therefore any apparent effect of the ultrasonication on the formation and phase of the synthesized KN powders, within a limit of the XRD technique.

The SEM images show the synthesized KN powders to compose mostly of lumber particles with a few fractions of pseudo-cubic particles, independent also on the preparative conditions. Figure 61 shows the representative images of the particles obtained from the reactions with and without the prior ultrasonication, illustrating well-defined shape from the reactions with the prior ultrasonication. Sizes of these KN particles measured directly from the SEM were distributed in a range of approximately 0.1-1 mm and 0.15-2.5 μm, for the short and long axes, respectively. In contrast, the particles with a serious melting and poor-defined particle boundary were obtained from the reactions conducted without the prior application of the ultrasonic wave.

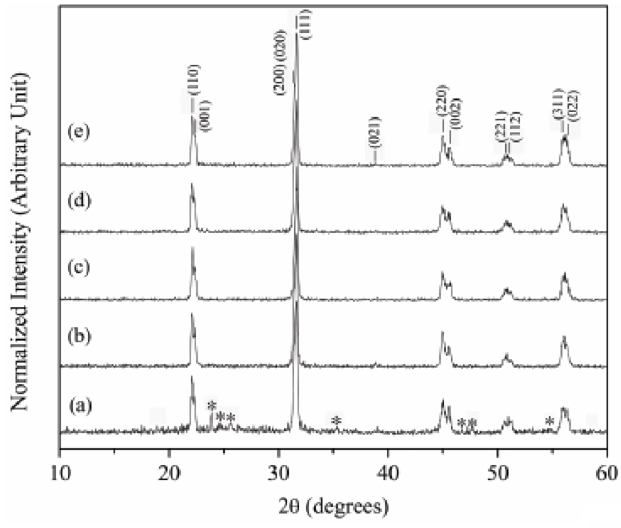

*__Fig. 59__ The XRD patterns of the powders obtained from the reactions conducted at 200 ^{o}C for (a) 1 h, (b) 3 h, (c) 6 h, (d) 12 h and (e) 24 h on the ultrasonicated mixtures; * indicates unidentified diffraction.*

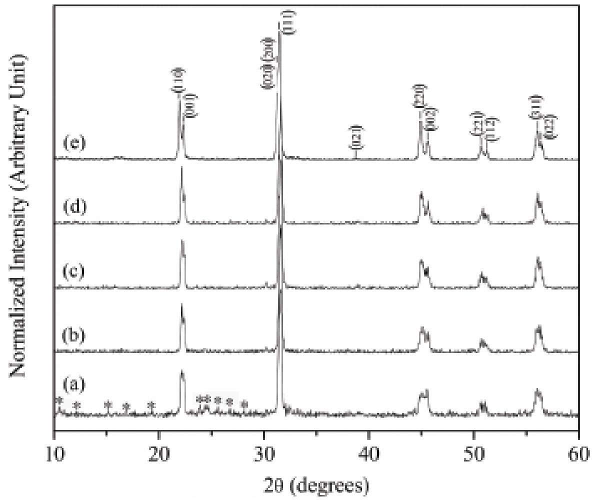

*__Fig. 60__ The XRD patterns of the powders obtained from the reactions conducted at 200 ^{o}C for (a) 1 h, (b) 3 h, (c) 6 h, (d) 12 h and (e) 24 h on the mixtures without the prior ultrasonication; * indicates unidentified diffraction.*

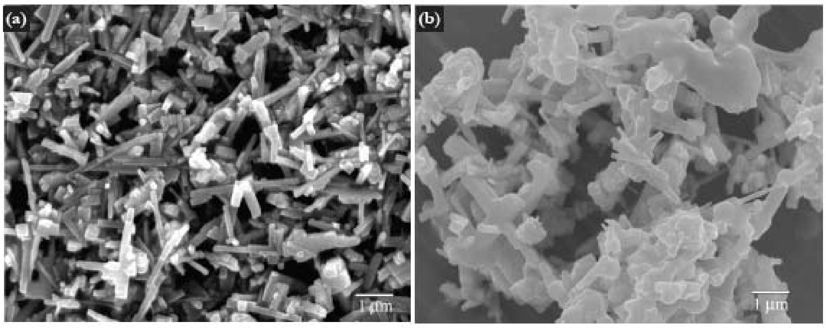

__Fig. 61__ The SEM images exemplifying the lumber particles of potassium niobate derived from the reactions on (a) the ultrasonicated reaction mixture and (b) the mixture without prior ultrasonication, conducted under the same synthesis conditions.

This may be rationalized by the ability of the ultrasonic wave in inducing the nucleation and in creation of the highly reactive and clean surface on the created nuclei which should promote the clean crystal growth in the afterward reactions [16]. The pressure generated under the solvothermal conditions generally causes the nucleation to occur as simultaneously as the crystal growth, which commonly results in hard aggregates [17].

In comparison to the former reports on the synthesis of KN fine powders using the hydrothermal reactions at the same temperature and KOH concentration of 200 ^{o}C and 8 mol dm^{-3}, several differences could be pointed out, although phase of the obtained KN is the same, which is the orthorhombic phase [14]. First, shape of the hydrothermally derived KN particles was largely pseudo-cubic, when the lumber particles could be obtained in this study. Second, sizes of the pseudo-cubic particles were also distributed in a larger size region of 1-4 mm, compared to the sub-micrometer sizes reported here. The use of mixed water-ethyl alcohol as a liquid medium apparently provided smaller sized and more elongated particles. Regarding the effective reaction, the employment of ethyl alcohol and the application of ultrasonic wave on the reaction mixtures did not result in any significant change.

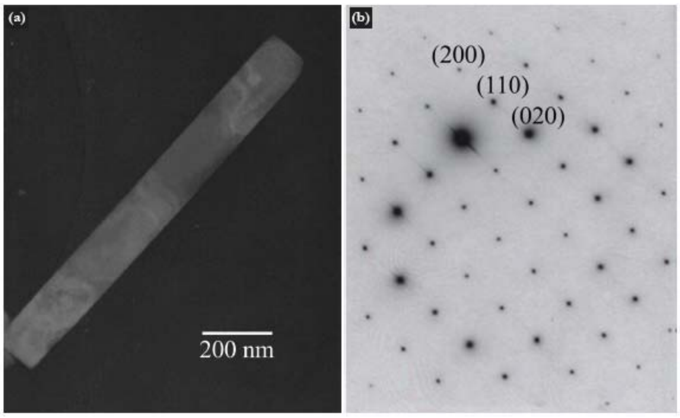

Fig. 62 *(a) The TEM image of the typical lumber potassium niobate particle with (b) the corresponding indexed SAED pattern based on the orthorhombic Cm2m (JCPDS 32-822).*

The structure of the lumber particles was also evaluated through selected area electron diffraction (SAED) in the transmission electron microscope. Figure 62 shows the TEM images of the typical particle and the corresponding SAED pattern, which could be well indexed in the assigned orthorhombic *Cm2m* phase. The growth direction apparently lied along the crystallographic [*110*] direction. The KN powders characterized by the XRD to be of the single orthorhombic phase were chosen for the sintering experiments, including those obtained from the reactions conducted for 3-24 h, both with and without the prior ultrasonication. After the sintering, the diameters and thickness of the sintered bodies were substantially reduced; 8.35-8.60 mm and 2.10-2.30 mm for the sintered pellets compared to 10.15 mm and 2.45-2.75 mm for the green bodies. The contraction in diameter of *ca.* 18% was slightly better than the contraction in thickness, *ca.* 14-16%. This corresponded to the volume shrinkage of *ca.* 36-42%. The densities of the sintered ceramics were measured, giving the results of *ca.* 95-98% in relative to the crystallographic density, 4.62 g cm^{-3}. No correlation between the obtained values and the variation in synthesis reaction time could be observed, although the powders obtained from the reactions with the prior ultrasonication showed slightly better volume shrinkage and densification. The shrinkage and relative densities of *ca*. 40-42% and 96-98%, respectively, could be calculated for the ultrasonication cases, when the shrinkage of 36-39% with the corresponding relative densities of *ca.* 95% were obtained for the other cases. This could be due to the better defined particle shape and less melting between the particles in the former case as revealed by the SEM images.

The SEM images taken on the sintered KN pellets gave supportive evidence, as exemplified in Fig. 63. The grain sizes of the sintered ceramic were measured and a slight growth of the sintered grain was revealed; 0.15-3.95 μm and 0.25-4.45 μm for the short and long axes. These results agree well with the calculated volume shrinkages and the calculated relative densities. It is apparent that the growth process occurred better along the short axis than the long axis, and resulted in an evolution of a pseudo-cubic grain from the pressurized lumber particles. It is also evident that the melting between grains was serious for the pellets which were prepared from the powders derived from prolonged solvothermal reaction, particularly those with the prior ultrasonication treatment. Regarding the hygroscopic problem commonly encountered with the sintering of KN [18], it was not the case in this study if the washing of the remaining alkali was performed carefully. The sensitivity to the atmospheric water may therefore attribute to the remaining of KOH which is hygroscopic.

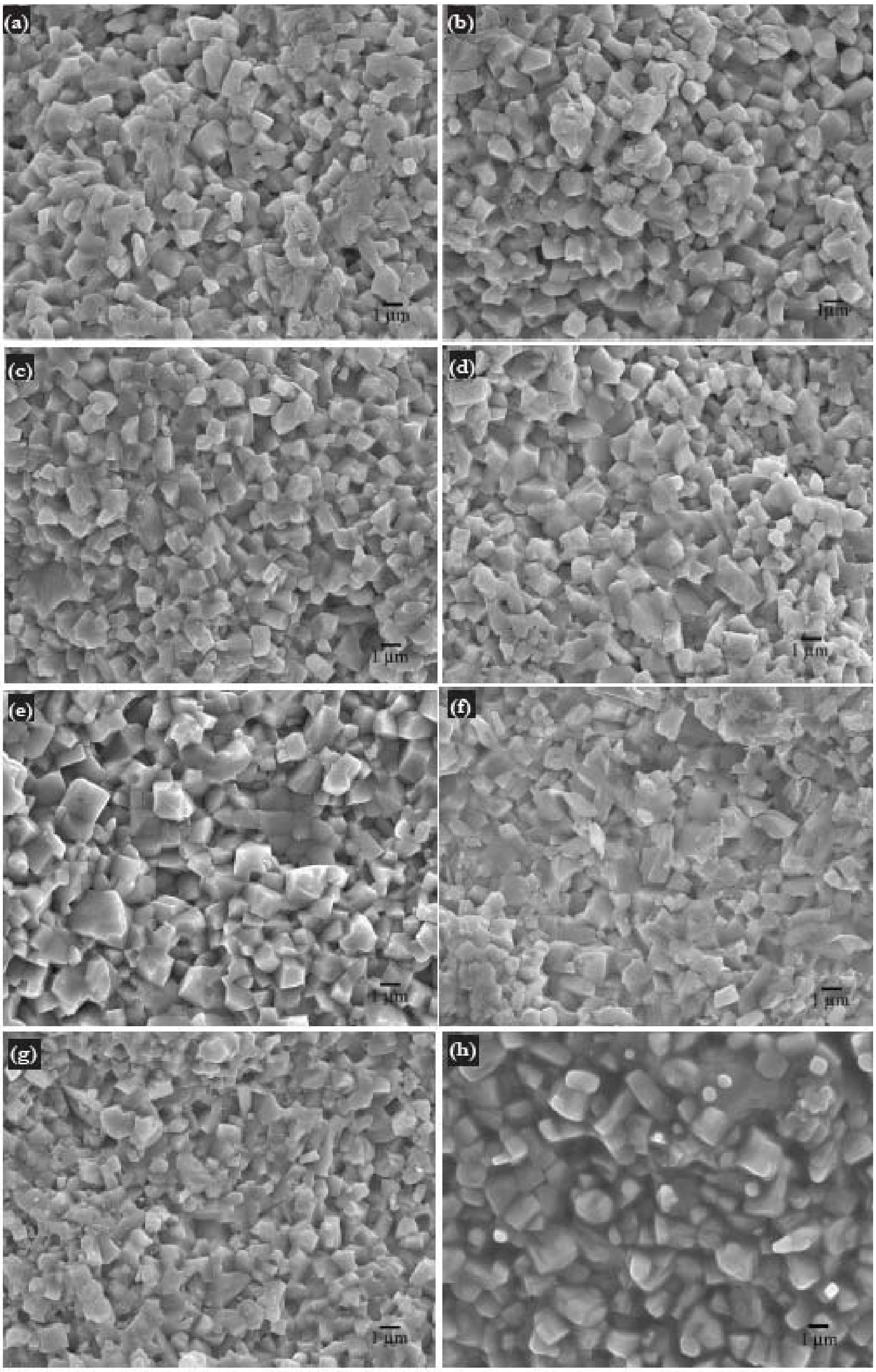

Fig. 63 *The SEM images of the sintered KN ceramics prepared from the powders obtained from the reactions conducted at 200 °C for (a) 3 h, (b) 6 h, (c) 12 h and (d) 24 h on the mixtures without the prior ultrasonication, compared with those of the sonicated mixtures; (e) 3 h, (f) 6 h, (g) 12 h and (h) 24 h.*

The XRD was used to follow the change in phase, if any, after the sintering and the results are shown in Figs. 64(a) and 65(a). The remaining of the orthorhombic KN was significant, although the formation of the niobium-rich phase, KNb_3O_8, suggesting the loss of K_2O during the sintering were evident. A develop of a big lump at low 2θ region was additionally plain, implying the corruption of the long range order in the structure although the distinction between the three most intense peaks, including (*020*), (*200*) and (*111*), were clearer after the sintering. The exception was apparent for the sintered pellets which were prepared from the powders obtained from 24 h reaction with the prior ultrasonication, where there was no signature of the KNb_3O_8 phase in the XRD pattern. This again reflects the merit of the application of the prior ultrasonication.

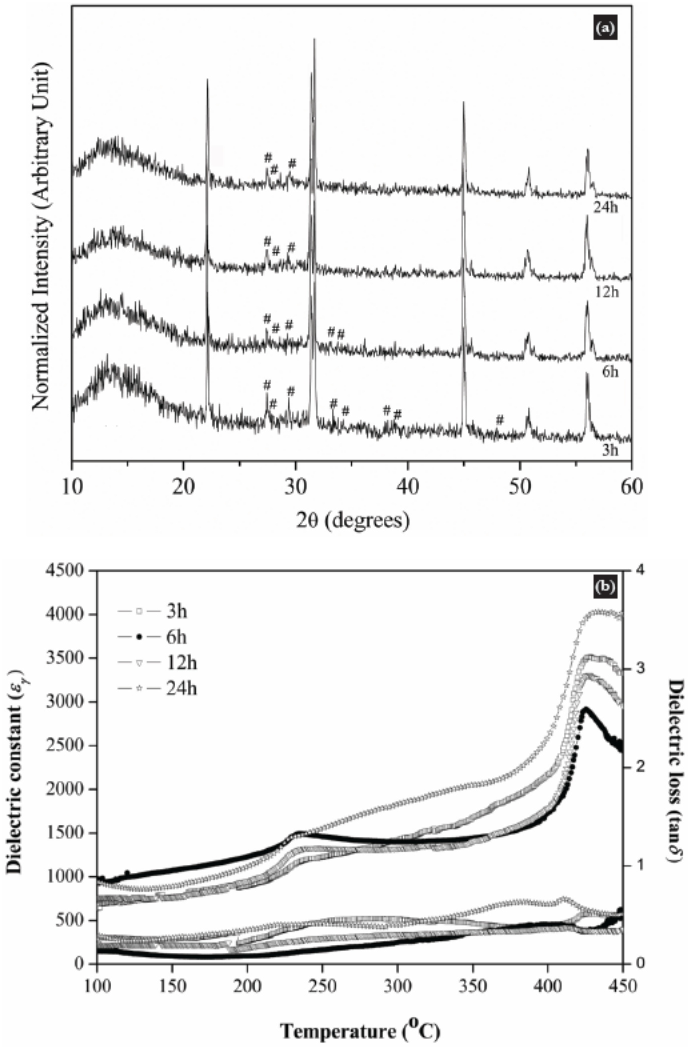

Fig. 64 *(a) The XRD patterns (# = KNb_3O_8) and (b) temperature dependence of dielectric properties measured on the KN ceramics prepared from the powders obtained from the reactions conducted at 200 ^{o}C for (a) 3 h, (b) 6 h, (c) 12 h and (d) 24 h on the mixtures without the prior ultrasonication.*

Figure 64(b) and Figure 65(b) show the temperature dependence of dielectric constants (εr) and dielectric loss tangents (tan δ) at 100 kHz for the sintered KN ceramics, revealing a difference in the measured values depending on the purity of KN according to the XRD patterns shown in the corresponding Fig. 64(a) and Fig. 65(a), respectively. Phase transition from the ideal cubic phase to the tetragonal phase was found around 425 ^{o}C, while the tetragonal to the orthorhombic occurred around 225 ^{o}C. The results are well consistent with the formerly reported values for the KN ceramics [18-21]. In the case of the ceramic composing of KN as nearly a single phase which was the one derived from the powders prepared from 3 h - 24 h reaction with the prior ultrasonication, the dielectric constants has increased with also a sharp peak transition, especially for the KN ceramics of high densities and good crystallinity. The KN ceramics which were fabricated from the powders prepared from the same conditions but without the prior ultrasonication, showed a broad peak transition, which should probably be due to the presence of the liquid phase in microstructure. This results were consistent with the XRD and SEM results that showed the formation of the second phase KNb_3O_8 and the liquid phase in the microstructure due to the evaporation of K_2O. In general, it was evident that the ceramics prepared from the powders which were derived from the reactions with the prior ultrasonication showed higher dielectric constants and lower dielectric loss than those without the prior ultrasonication. This may attribute to the increase in oxygen vacancies which on the other hand contribute to the increase in conductivity [22].

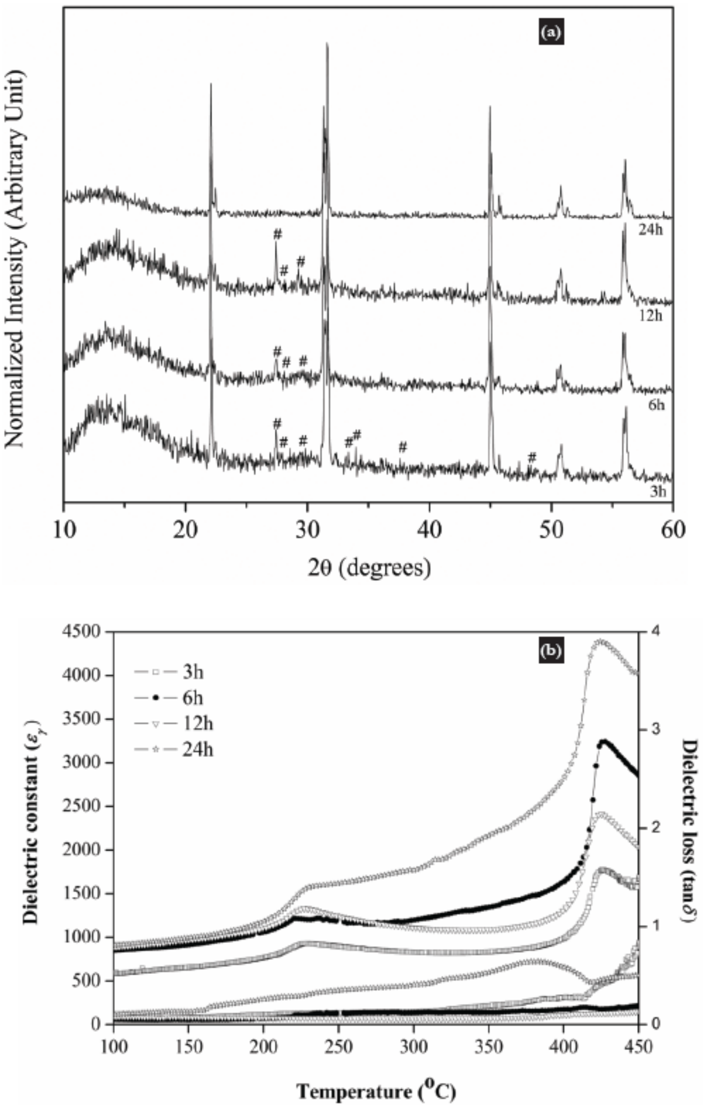

Fig. 65 *(a) The XRD patterns (# = KNb_3O_8) and (b) temperature dependence of dielectric properties of the KN ceramics prepared from the powders obtained from the reactions conducted at 200 °C for (a) 3 h, (b) 6 h, (c) 12 h and (d) 24 h on the mixtures with the prior ultrasonication.*

CONCLUSIONS

In summary, the sonocatalyzed ethanothermal process has been attempted with the synthesis of potassium niobate fine powders, and proved to be able to provide the orthorhombic phase-pure KN powders under mild condition and rapid reaction times of at least 3 h. The use of mixed water-ethyl alcohol liquid medium apparently favoured the formation of elongated lumber KN particles of sub-micrometer sizes, when the application of the prior ultrasonication on the reaction mixtures led to significant differences in sintering behavior, loss of K_2O and the tolerance of the orthorhombic KN to the sintering, as well as the corresponding dielectric properties. Dense KN ceramics of over 95% relative densities could be fabricated by conventional sintering without the hygroscopic problem. The significance of the prior ultrasonication on the reaction mixtures during the synthesis in enhancing both physical and electrical properties of the sintered ceramics was clearly illustrated.

REFERENCES

1. K. Kakimoto, I, Masuda, And H. Ohsato, *J. Euro. Ceram. Soc.* **25** (2005) 2719-2722.
2. K. Tanak, K.I. Kakimoto and H. Ohsato, *J. Euro. Ceram. Soc.* **27** (2007) 3591-3595.
3. I. Pribosic, D. Makovec and M. Drofenik, *J. Euro. Ceram. Soc.* **25** (2005) 2713-2717.
4. R. Yang, S.Y. Shen, C.B. Wang, W. Shen and L.M. Zhang, *Thin Solid Films* **516** (2008) 8559-8563.
5. H. Muthurajan, H.H Kumar, V. Samuel, U.N. Gupta and V. Ravi, *Ceram. Int.* **34** (2008) 671-673.
6. T. Su, H. Jiang, H. Gong, Y. Zhai, *J. Mater. Sci.* **45** (2010) 3778-3783.
7. U. Fluckiger, H. Arend, H.R. Oswald, *Am. Ceram. Soc. Bull.* **56** (1977) 575-577.
8. N. Kumada, T. Kyoda, Y. Yonesaki, T. Takei and N. Kinomura, *Mater. Res. Bull.* **42** (2007) 1856-1862.
9. J.W. Liu, G. Chen, Z.H. Li. and Z.G. Zhang, *Int. J. Hydrogen Energy* **32** (2007) 2269-2272.
10. W.L. Suchanek, *Chem. Mater.* **16** (2004) 1083-1090.
11. K. Kajiyoshi, K.Yanagisawa, Q. Feng and M. Yoshimura, *J. Mater. Sci.* **41** (2006) 1535-1540.
12. M. Kosec, D. Kolar, *Mater. Res. Bull.* **10** (1975) 335-340.
13. I. Pribo, D. Makovec, M. Drofenik, *J.Mater. Res.* **17** (2002) 2989-2992.
14. Lu C.H., Lo S.Y., Lin H.C., *Mater. Lett.*, 1998; **34**: 172-176.
15. R. Morrel, Handbook of properties of technical & engineering ceramics, *HMSO Publications*, London (1989).
16. K.S. Suslick, *Science* **247** (1990) 1439-1445.
17. R.E. Riman, W.L. Suchanek and M.M. Lencka, *Ann. Chim. Sci. Mat.* **27** (2002) 15-21.
18. K. Matsumoto, Y. Hiruma, H. Nagata and T. Takenaka, *Ferroelectrics* **358** (2007) 169-174.
19. M. Ishikawa, N. Takiguchi, H. Hosaka and T. Morita, *Jpn. J. Appl. Phys.* **47** (2008) 3824-3828.
20. C.K.Tan, G.K.L. Goh and W.L. Cheah, *Thin Solid Films* **515** (2007) 6577-6581.
21. M. Ishikawa, Y. Kadota, N. Takiguchi, H. Hosaka and T. Morita, *Jpn. J. Appl. Phys.* **47** (2008) 7673-7677.
22. G. Singh, V.S. Tiwari and P.K. Gupta, *J. Appl. Phys.* **107** (2010) 064103.

APPENDIX

REPRINTS OF THE PUBLISHED ARTICLES

A1

J Inorg Organomet Polym (2009) 19:306–313
DOI 10.1007/s10904-009-9271-y

Microwave Assisted Crystal Growth of a New Organic—Decavanadate Assembly: $[V_{10}O_{27}(OH)] \cdot 2(C_6N_2H_{14}) \cdot (C_6N_2H_{13}) \cdot (C_6N_2H_{12}) \cdot 2H_2O$

Bunlawee Yotnoi · Saranphong Yimklan ·
Timothy J. Prior · Apinpus Rujiwatra

Received: 13 October 2008 / Accepted: 1 April 2009 / Published online: 14 April 2009

Abstract Microwave synthesis was used to grow single crystals of a new organic–inorganic supramolecular assembly, $[V_{10}O_{27}(OH)] \cdot 2(C_6N_2H_{14}) \cdot (C_6N_2H_{13}) \cdot (C_6N_2H_{12}) \cdot 2H_2O$, in a very short time compared to the conventional solution technique. In order to generate crystals suitable for single crystal experiments, an equimolar mixture of reactants and a few hours of microwave heating are required. Although non-merohedral twinning is an inherent problem, the crystal structure can be solved and refined in the orthorhombic space group *Pna2₁* with $a = 20.972(4)$ Å, $b = 10.3380(14)$ Å, $c = 20.432(3)$ Å, $Z = 4$, with an excellent result, $R(F^2) = 0.0431$. The assembly is hydrogen bond-assisted and built up of the monoprotonated decavanadate and 1,4-diazabicyclo[2.2.2]octane of various degrees of protonation. The number and location of protons on both the inorganic and organic motifs govern the formation of the extensive hydrogen bonding network, which in turn regulates the assembly architecture.

Keywords Single crystal growth · Microwave synthesis · Decavanadate · Supramolecular assembly · Hydrogen bond

1 Introduction

Polyoxometallates (POMs) are one of the best known classes of complex anions and these continue to attract interest from both scientists and technologists. This is due to the diversity and richness in their chemistry and physics, which have led to a rapid expansion in the number of potential applications [1–3]. Among the well studied POMs, polyoxovanadates (POVs) compose a unique class, displaying a distinct potential for biology, materials science and medicinal applications [4–7]. The usage of these POVs, and decavanadates in particular, as structural building units in the synthesis of high dimensional hydrogen bond-assisted supramolecular assemblies composed of both inorganic and organic components such as $[H_2V_{10}O_{28}](C_{20}N_8H_{32})(H_2O)_4$, $[(C_2H_5)_3NH]_4[H_2V_{10}O_{28}]$, $(C_4N_2S_2H_{14})_2[H_2V_{10}O_{28}]$ and $[\boldsymbol{C211}H_2]_2[H_3O]_2[V_{10}O_{28}] \cdot 7H_2O$ where ***C211*** is a cryptand, is however still scattered [8–12]. The supramolecular arrangement of these compounds depends strongly on the abundance and locations of protonation sites on the decavanadates, and the nature of the organic molecules. These factors can impart immense influence *via* the synergistic interplay of Coulombic, van der Waals and hydrogen bonding interactions. While the structure of the decavanadate is well documented [8], the choice of organic molecules and synthetic conditions can be varied and these are therefore of utmost importance in directing the supramolecular organization.

All previous reports of organic—decavanadate assemblies describe direct crystallization from solution under either ambient or hydro/solvothermal conditions. These reactions commonly require days or weeks to afford single crystals suitable for complete structural characterization. Recently microwave synthesis has been utilized in the synthesis of inorganic and inorganic–organic hybrid materials as well as ceramics, following the demonstration of tremendous advantages of this technique in organic synthesis [13–16]. The application of the technique in the growth of single crystals of inorganic–organic hybrid compounds is

---

B. Yotnoi · S. Yimklan · A. Rujiwatra (✉)
Department of Chemistry, Faculty of Science, Chiang Mai University, Chiang Mai 50200, Thailand
e-mail: apinpus@chiangmai.ac.th

T. J. Prior
Department of Chemistry, University of Hull,
HU6 7RX Kingston upon Hull, UK

A2

however novel. The fast kinetics of microwave reactions may shorten the reaction times, although this can induce disorder in the structure and hence hinder the growth of single crystals which generally requires very high degree of internal order.

Here we introduce the usage of microwave technique for a rapid single crystal growth of a new three dimensional hydrogen-bond assisted supramolecular assembly, based on the decavanadate monomer and 1,4-diazabicyclo[2.2.2]octane. Structural characterization based on single crystal X-ray diffraction data and synergistic interactions analysis is reported.

2 Experimental

2.1 Microwave—Assisted Crystal Growth and Spectroscopic Characterization

Crystals of $[V_{10}O_{27}(OH)] \cdot 2(C_6N_2H_{14}) \cdot (C_6N_2H_{13}) \cdot (C_6N_2H_{12}) \cdot 2H_2O$ (**1**) were readily grown from aqueous reactions between V_2O_5 and 1,4-diazabicyclo[2.2.2]octane (DABCO). In a typical experiment, a mixture of 0.4044 g of V_2O_5 (Fluka 98.0%) and 0.2492 g of DABCO (Fluka 95.0%) was prepared in 9.00 mL deionized water, giving a molar ratio of 1:1:225. The mixture was stirred vigorously for 30 min at ambient temperature and pressure, before being transferred into an 18 mL Teflon reactor. The reactor was then placed in a 95(±5) °C water bath, covered with a polypropylene cover and located in a domestic microwave oven (Whirlpool XT-25ES/S, 900 W, 2.45 GHz). Although the microwave power can be adjusted to a full range of 100%, reactions were conducted under autogenous pressure using a constant power of 70% (630 W) for varying duration between 1- and 3-h. After the microwave power was switched off, the reaction was cooled down to room temperature in a conventional oven using a cooling rate of 0.5°C/min. Due to the static model of the reactor, the temperature inside the reactor was not measured, and it should be referred to solely by the employed microwave power. The solid products were separated from the supernatant solution by filtration, washed with deionized water and dried in air. Yields of the synthesized solid products were typically *ca.* 60% based on the V_2O_5. Size and habit of the crystals were examined using a field-emission scanning electron microscope (FESEM: JEOL JSM-6335F). In order to study the influence of DABCO on the formation of **1**, the V_2O_5:DABCO molar ratio was varied from 1:0.5 to 1:1.5. The pH of each mixture was measured before and after each reaction using a pH meter (Metrohm Siam Model 744). No attempt to adjust the pH of reaction mixtures prior to synthesis was carried out.

The crystals of **1** were separated under optical microscope from the solid product of the reaction using an equimolar V_2O_5:DABCO ratio and 2 h of microwave heating, and ground for further experiments. Elemental analysis was performed using a Perkin Elmer Series II 2400 CHN/S analyzer. Infrared spectra were collected on a Bruker Tensor 27 FT - IR instrument (4000–400 cm^{-1}, resolution 0.5 cm^{-1}) using a KBr (BDH 98.5%) pellet. The UV spectrum of **1** was collected on a Perkin Elmer UV LAMDA 25 spectrophotometer. The X-ray powder diffraction (XRD) pattern was collected using a Bruker D8 Advance diffractometer, operating with a Ni filtered Cu K_α radiation ($\lambda = 1.540558$ Å, 48 kV and 30 mA).

2.2 X-Ray Crystal Structure Determination

A number of batches of products were examined and apparently crystalline material was present in all of them. Crystals of two morphologies were identified from the reaction using a V_2O_5:DABCO ratio of 1:1; namely hexagonal plates and rhombic bars. A large number of crystals were of examined. The plates were frequently found to be twinned with diffraction images showing the presence of multiple crystallites. Full data sets were collected from two such crystals and afforded moderate quality solutions on account of unresolved twinning. The rhombic bars were not subject to the same accidental twinning and diffraction images did not suggest the presence of multiple crystallites. Data were collected from an orange bar of size 0.1 × 0.05 × 0.05 mm^3 at 150(2) K using a Stöe IPDS2 image plate diffractometer operating with Mo Kα radiation using a single ω—scan. Crystals were cooled using an Oxford Instruments nitrogen gas cryostream. The faces of the crystal were indexed and an analytical absorption correction applied to the data.

Systematic absences in the data suggested one of two orthorhombic space groups, either *Pna2₁* (no. 33, non–centrosymmetric) or *Pnam* (no. 62, centrosymmetric). It was not possible to solve the structure in *Pnam* but routine automatic Direct Methods implemented within SHELXS-93 [17] located all non-hydrogen atoms in the structure in *Pna2₁*. Following completion of the structure by using SHELXL-97 [18], there was no evidence for additional symmetry found by PLATON [19]. The crystal examined was found to be racemically twinned with two roughly equal components, but there was no evidence that the true symmetry of the structure was centrosymmetric. Data were weak but the final refinement converged with excellent R-factors ($R_1 = 0.0431$) with a structure very similar to that obtained from the hexagonal plates. Hydrogen atoms in the organic components were located in final difference Fourier maps. These were placed at geometrically calculated positions. Hydrogen atoms on water and the amine

A3

functionality of the DABCO were placed so as to generate chemically sensible hydrogen bonds where necessary. The balancing of charge suggested the decavanadate unit bears a single proton. The protonation site was determined from Bond Valence Sum (BVS) calculations [20, 21].

3 Results and Discussion

3.1 Microwave—Assisted Crystal Growth and Spectroscopic Characterization

In the synthesis and crystal growth of **1**, microwave heating has been proved to afford crystals suitable for single crystal diffraction experiments, although twinning seems to be common. Non-merohedral twinning may be an inherent drawback. This may be due to the fast mass transport near surface and/or at structural interface associated with the growth of the crystals, which is known to induce disorder to the growth [16]. Variation of the V_2O_5:DABCO molar ratio from 1:0.5 to 1:1.5, which results in slightly different pH—6.44, 6.52 and 6.58 for 1:0.5, 1:1 and 1:1.5, respectively,—evidently led to different phase formation using the same microwave heating time of 3 h. Figure 1 shows the XRD patterns of the solid products synthesized using different V_2O_5:DABCO molar ratio (Fig. 1d–f) in comparison to the simulated pattern of **1** (Fig. 1a). It can be clearly seen that the usage of equimolar V_2O_5:DABCO ratio (Fig. 1d) provides the nearly phase-pure product of **1**. The SEM micrographs of the crystals obtained from this reaction show two crystal habits—hexagonal plates and rhombic bars (Fig. 2a, b), the single crystal experiments, however, reveal the common crystal structure. The deviation of the V_2O_5:DABCO ratio from the equimolar

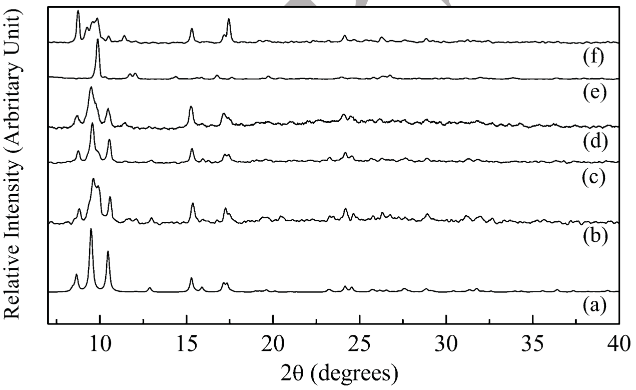

Fig. 1 The powder XRD patterns of the products obtained from the reactions using 1:1 V_2O_5:DABCO but different reaction time—(b) 1 h, (c) 2 h and (d) 3 h—and a constant 3 h of microwave heating but different V_2O_5:DABCO molar ratio—(d) 1:1, (e) 1:0.5 and (f) 1:1.5—in comparison to (a) the simulated pattern of **1**

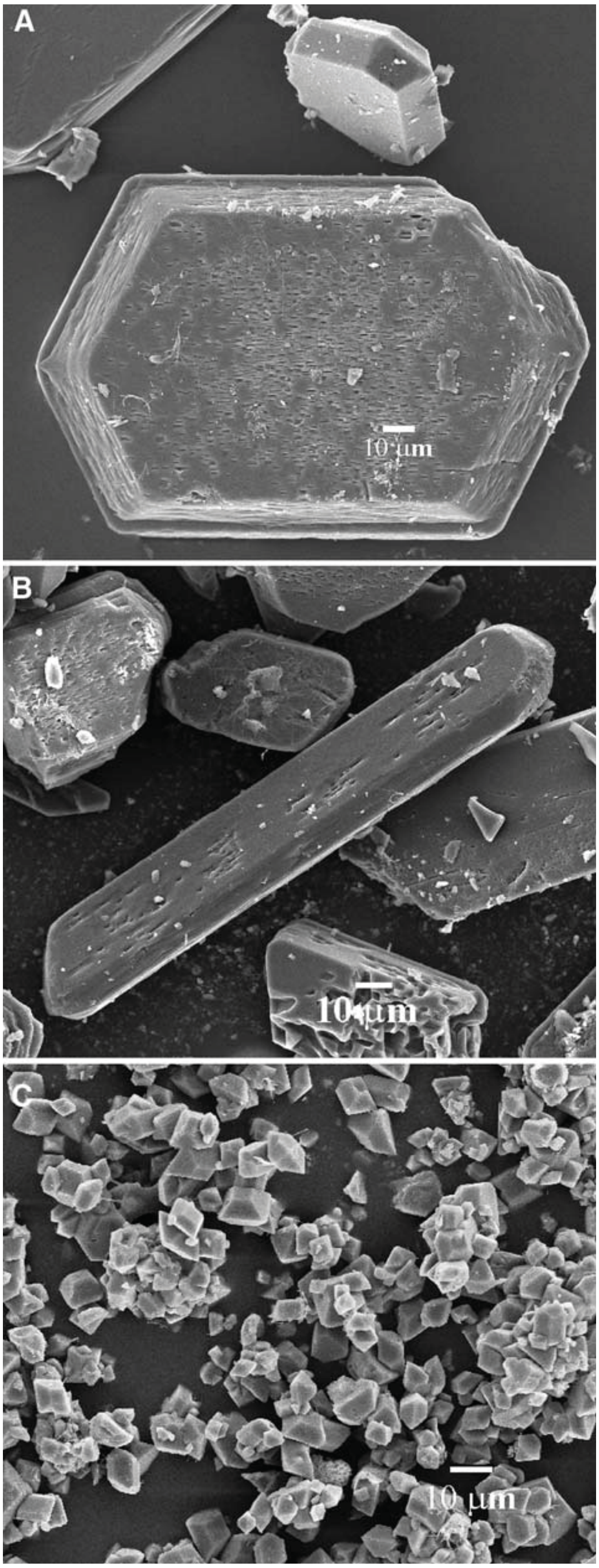

Fig. 2 SEM micrographs showing different crystals habits in the products obtained from the reactions using different V_2O_5:DABCO molar ratios—**a** and **b** 1:1, and **c** 1:1.5

A4

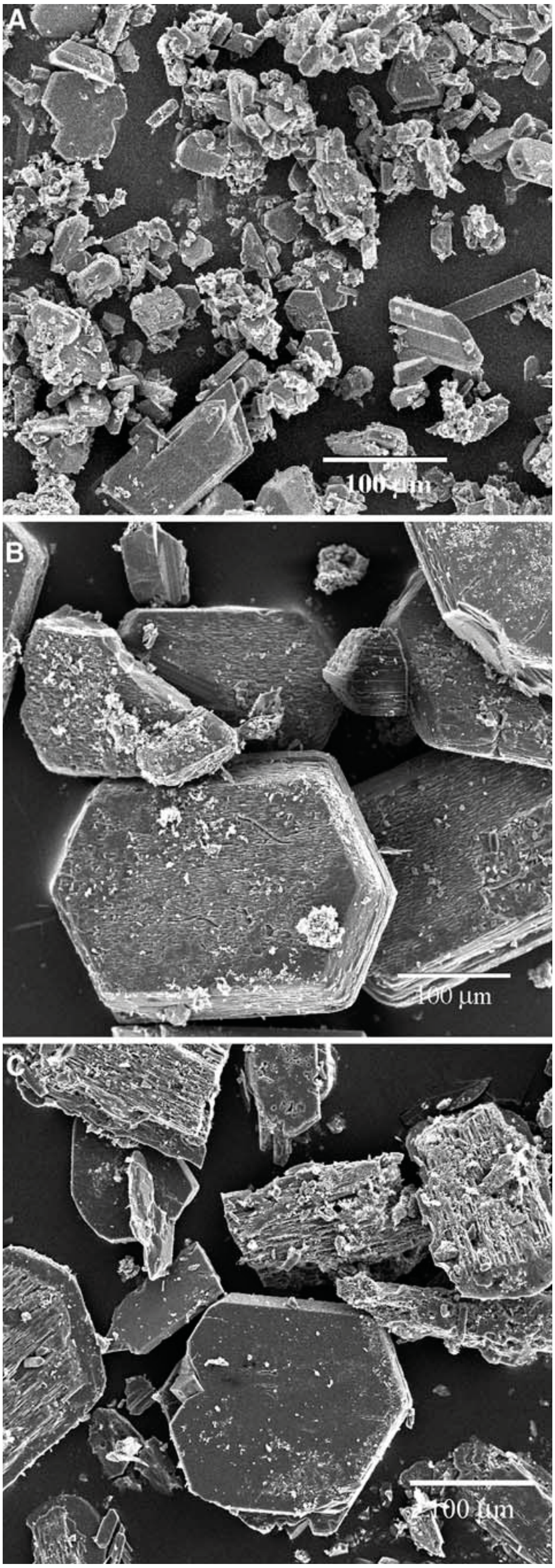

◀ **Fig. 3** SEM micrographs showing different crystals habits and size in the products obtained from the reactions using an equimolar V_2O_5:DABCO molar ratio but different microwave heating time—**a** 1 h, **b** 2 h and **c** 3 h

stoichiometry results in the formation of the totally different phases (Fig. 1e, f) of possibly layer structures. These phases could not be identified due to the insufficient number of the diffraction peaks. The SEM micrographs of the crystals obtained from the reaction using 1:0.5 and 1:1.5 of V_2O_5:DABCO accordingly reveal different crystal habit of truncated octahedra of relatively smaller sizes as illustrated in Fig. 2c.

Based on the XRD result (Fig. 1b–c), a reduction of microwave heating time to 2 h gave similar result of a nearly phase-pure **1.** This indicates the formation of **1** to commence as a dominant phase since the first 2 h of microwave heating. SEM photographs (Fig. 3) reveal the crystals obtained from the reaction employing 2 h of microwave heating to be larger and better quality than those from the 3 h duration synthesis. A reduction of the microwave reaction time to 1 h however resulted in a mixed product of **1** and the other unidentified phase. Sizes

Table 1 Crystallographic data for structural solution and refinement of **1**

CCDC no.	688180
Formula	$[V_{10}O_{27}(OH)] \cdot 2(C_6N_2H_{14}) \cdot (C_6N_2H_{13}) \cdot (C_6N_2H_{12}) \cdot 2H_2O$
Formula weight	1448.18
Crystal size/mm^3	$0.1 \times 0.05 \times 0.05$
Crystal system	Orthorhombic
Space group	*Pna2$_1$*
a/Å	20.972(4)
b/Å	10.3380(14)
c/Å	20.432(3)
V_{cell}/Å^3	4429.83(12)
Z	4
ρ_{calc}/gcm^{-3}	2.171
T/K	150(2)
Radiation (λ/Å)	Mo (0.71073)
μ/mm^{-1}	2.117
θ_{min}, θ_{max}	1.94, 26
Total data	8693
Unique data	3451
Parameters no.	665
Restraints no.	272
Goodness of fit	0.643
R(F^2), R$_w$ (all data)	0.1395, 0.0878
R(F^2), R$_w$($I > 2\sigma(I)$)	0.0431, 0.0674

A5

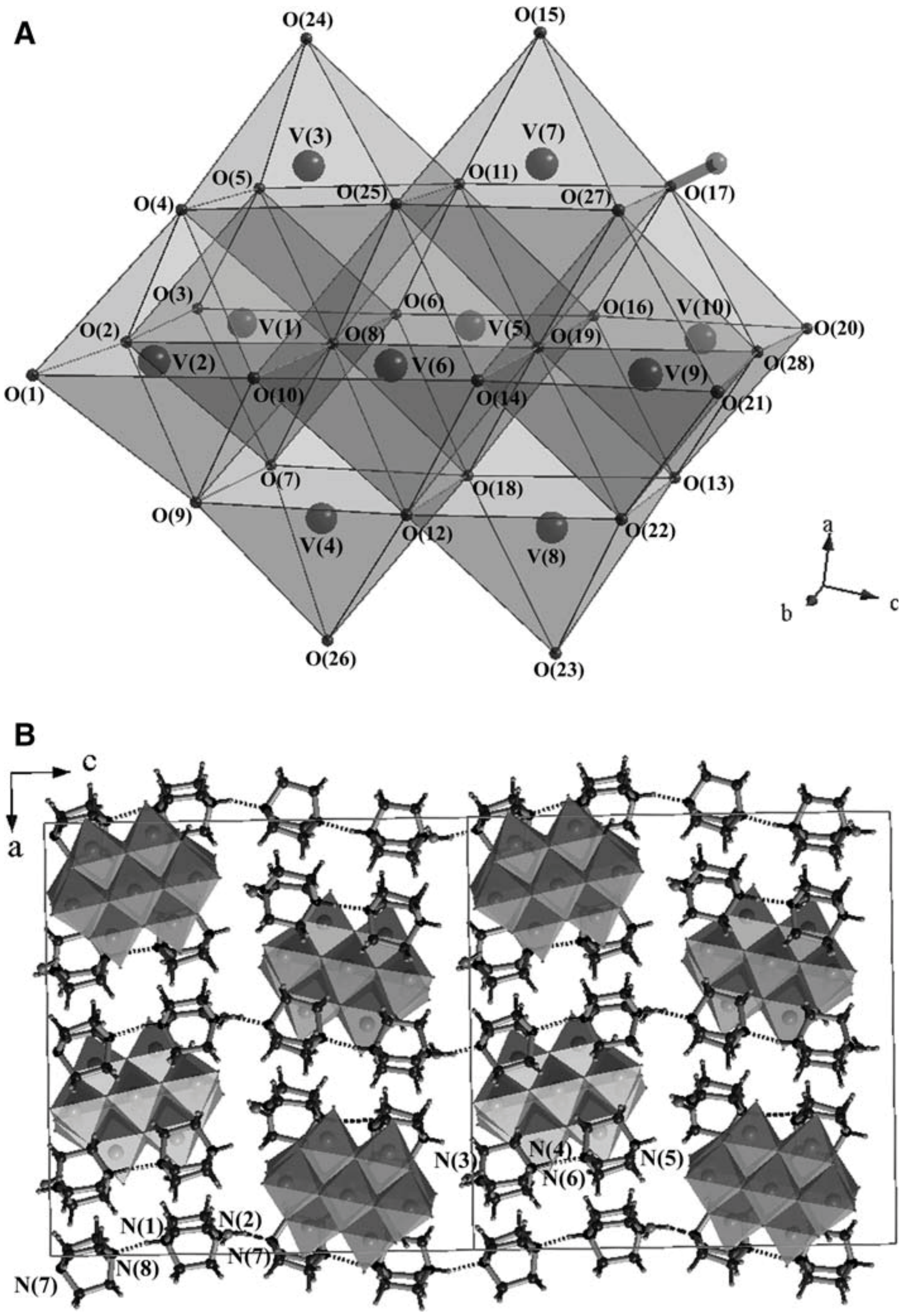

Fig. 4 **a** Polyhedral representation of the decavanadate complex anion and **b** the spatial arrangement of the decavanadate and the DABCO molecules/ions viewed along the *b*-axis

of the obtained crystals were also smaller than the other cases and the morphology was irregular. The single crystal experiments were then conducted on the crystals chosen from the reaction using equimolar stoichiometry of V_2O_5:DABCO and 2 h of microwave heating. A reduction in the synthesis time required for the growth of single crystals of appropriate quality for full structure determination from days or weeks to only a few hours demonstrates the possible advantage of microwave synthesis. The current study indicates the induced kinetic enhancement in the growth of single crystals of new compounds in an inorganic—organic hybrid system. The phase purity, crystal quality and crystal size depend, however, on both the reagent stoichiometry and microwave heating time.

The UV spectrum of **1** exhibited an intense and broad peak at 204-227 nm, which can be ascribed to the O → V charge transfer band, and in accordance with the existence of the decavanadate monomer. The elemental analysis shows an acceptable agreement between the experimental and the calculated figures: element, %calc. (%found): C, 19.89(20.19(5)); N, 7.73 (6.97(7)). The FT-IR spectrum also affirms the presence of the functionalities in **1** (frequency assignment, cm^{-1}): ν(N–H), 3436 s; ν(C–H), 3015 m; δ_{as}(N–H), 1616 m; δ(C–H), 1466 m; δ_s(N–H),

A6

1338 m; ν(C–N), 1056 m; ν_s(V–O$_T$), 956vs; ν_{as}(V–O$_T$), 835vs; ν_s(V–O$_b$–V), 750 s; ν_{as}(V–O$_b$–V), 619 s.

3.2 Crystal Structure Determination of 1

The structure of **1** determined by single crystal diffraction has the empirical formula, $[V_{10}O_{27}(OH)] \cdot 2(C_6N_2H_{14}) \cdot (C_6N_2H_{13}) \cdot (C_6N_2H_{12}) \cdot 2H_2O$, and is built up from the following building units: a monoprotonated decavanadate cation $[V_{10}O_{27}(OH)]^{5-}$, two water molecules, and three different types of the organic moieties, including two diprotonated H$_2$DABCO^{2+}, a monoprotonated HDABCO^{+} and a neutral DABCO molecule. Crystal data for **1** are summarized in Table 1. The decavanadate anion comprises ten crystallographically distinct vanadium atoms. These all adopt a distorted coordination octahedral geometry (Fig. 4a), which are connected *via* edge-sharing. Four distinct types of oxygen coordination are present; these can be classified as the bridging μ6-O (O8, O19), μ3-O (O11, O12, O18, O25), μ2-O (O2, O4, O5, O6, O7, O9, O10, O13, O14, O16, O17, O22, O27, O28) and the terminal oxygen O$_T$ (O1, O3, O15, O20, O21, O23, O24, O26) [8]. The bond lengths and angles found in the decavanadate anion are in good accordance with those found in previously reported decavanadate structures [10–12]. The BVS calculations based on the refined bond lengths listed in Table 2 suggest the pentavalence of vanadium, V^{V}, and the under-bonded character of O17 (BVS = 1.35) is indicative of the protonation site. Table 3 summarizes the calculated BVS results. The location of a single proton determined by BVS calculations corresponds well with the slight acidity of the reaction mixture promoting the protonation and a known tendency of the decavanadate-to-oxygen atom basicity where μ2-O and μ3-O are the most probable atoms to be protonated [8]. The existence of the protonation is also supported by the formation of the hydrogen bonding network in **1**, which is discussed later in detail. The monoprotonated decavanadate, $[V^{V}_{10}O_{27}(OH)]^{5-}$, is accordingly composed of two [V(μ2-O)$_2$(μ3-O)$_2$(μ6-O)$_2$] (V5, V6), four [VO$_T$(μ2-O)$_2$(μ3-O)$_2$(μ6-O)] (V3, V4, V7, V8) and four [VO$_T$(μ2-O)$_4$(μ6-O)] (V1, V2, V9, V10). The existence of only the fully oxidized V^{V} suggests that under the conditions employed DABCO is stable. This is intriguing because the reactions between V$_2$O$_5$ and organodiamines, including

Table 2 Selected bond lengths (Å) with their standard deviations in brackets for **1**

O1–V2	1.589(10)	O15–V7	1.582(9)	C3–C4	1.561(15)
O2–V1	1.829(10)	O16–V5	1.704(9)	C4–N1	1.469(16)
O2–V2	1.838(10)	O16–V10	1.986(9)	C5–N1	1.488(16)
O3–V1	1.605(9)	O21–V9	1.595(8)	C5–C6	1.512(15)
O4–V3	1.828(9)	O22–V8	1.812(9)	C6–N2	1.477(15)
O4–V2	1.880(9)	O22–V9	1.819(9)	C31–N3	1.509(17)
O5–V3	1.802(9)	O23–V8	1.586(9)	C31–C32	1.547(14)
O5–V1	1.846(8)	O24–V3	1.575(9)	C32–N4	1.483(15)
O6–V5	1.670(8)	O25–V7	1.931(9)	C33–N4	1.488(16)
O6–V1	2.082(8)	O25–V6	1.926(10)	C33–C34	1.548(14)
O7–V4	1.805(9)	O25–V3	2.029(9)	C34–N3	1.467(15)
O7–V1	1.902(9)	O26–V4	1.576(9)	C35–N3	1.469(16)
O8–V5	2.086(10)	O27–V7	1.851(9)	C35–C36	1.540(15)
O8–V6	2.093(10)	O27–V9	1.933(9)	C36–N4	1.469(16)
O8–V3	2.237(9)	O28–V9	1.844(9)	C55—N6	1.472(15)
O8–V4	2.251(9)	O28–V10	1.854(9)	C55–C56	1.527(15)
O8—V1	2.351(9)	O17–V7	1.916(9)	C51–N5	1.473(15)
O8–V2	2.344(9)	O17–V10	1.984(9)	C51–C52	1.544(15)
O9–V4	1.812(8)	O18–V5	1.930(1)	C52–N6	1.478(16)
O9–V2	1.840(9)	O18–V8	1.960(9)	C53–N6	1.487(16)
O10–V6	1.688(9)	O18–V4	2.017(8)	C53–C54	1.544(15)
O10–V2	2.038(9)	O19–V6	2.115(11)	C54–N5	1.501(17)
O11–V5	1.915(9)	O19–V5	2.135(10)	C56–N5	1.510(16)
O11–V7	1.988(8)	O19–V7	2.263(10)	C71–N7	1.482(15)
O11–V3	2.015(8)	O19–V8	2.241(10)	C71–C72	1.540(16)
O12–V6	1.929(9)	O19–V9	2.281(10)	C72–N8	1.484(16)
O12–V8	1.940(9)	O19–V10	2.307(10)	C73–N8	1.447(18)
O12–V4	2.023(9)	O20–V10	1.601(10)	C73–C74	1.577(17)
O13–V10	1.783(10)	C1–N1	1.495(17)	C74–N7	1.457(16)
O13–V8	1.885(9)	C1–C2	1.532(15)	C75–C76	1.549(15)
O14–V6	1.696(8)	C2–N2	1.495(15)	C75–N7	1.493(16)
O14–V9	2.034(9)	C3–N2	1.445(15)	C76–N8	1.483(16)

Table 3 Calculated BVS for vanadium and oxygen atoms involving decavanadate anion

Atom	BVS	Atom	BVS
V1	4.99	V6	5.02
V2	5.17	V7	5.03
V3	5.21	V8	5.23
V4	5.23	V9	5.12
V5	5.06	V10	5.13
μ2-O2	1.84	μ6-O8	1.99
μ2-O4	1.75	μ6-O19	1.96
μ2-O5	1.89	μ3-O11	1.91
μ2-O6	1.90	μ3-O12	1.95
μ2-O7	1.76	μ3-O18	1.92
μ2-O9	1.88	μ3-O25	1.97
μ2-O10	1.89	O1$_T$	1.78
μ2-O13	1.86	O3$_T$	1.71
μ2-O14	1.87	O15$_T$	1.82
μ2-O16	1.92	O20$_T$	1.73
μ2-O17	1.35	O21$_T$	1.75
μ2-O22	1.93	O23$_T$	1.78
μ2-O27	1.58	O24$_T$	1.85
μ2-O28	1.77	O26$_T$	1.85

A7

Table 4 Distances (Å) and angles (°) involving hydrogen bonds for **1**

D	A	H···A	D···A	∠D–H··A
N1	N8	1.76	2.682(12)	170
O1w	O20	2.24(8)	2.963(14)	152(8)
N2	N7#2	1.84	2.729(13)	160
O1w	O7#7	2.09(9)	2.855(12)	147(9)
O1w	O9#7	2.53(9)	3.263(12)	142(8)
N3	O28#5	1.76	2.657(12)	161
O2w	O4	2.14(5)	2.910(13)	146(8)
N4	N6	1.72	2.649(12)	176
O2w	O27#8	2.21(9)	2.960(14)	139(7)
N5	O1w	2.19	2.938(13)	137
N5	O2#7	2.13	2.818(12)	129
O17	O2w#1	2.11(9)	2.926(13)	177(11)
C1	O27#3	2.50	3.328(16)	140
C1	O23#4	2.42	3.102(17)	125
C2	O23#4	2.46	3.108(15)	123
C2	O21#3	2.36	3.223(15)	145
C3	O21#3	2.38	3.219(16)	142
C3	O20	2.49	3.268(16)	135
C4	O17	2.44	3.207(17)	134
C4	O14#3	2.41	3.358(17)	159
C5	O23#4	2.59	3.199(15)	119
C5	O15	2.57	3.544(15)	169
C6	O23#4	2.42	3.121(15)	127
C31	O1#3	2.50	3.174(16)	125
C31	O3	2.49	3.222(17)	131
C32	O6	2.43	3.363(15)	157
C32	O9#3	2.49	3.274(15)	136
C33	O24#6	2.50	3.156(17)	123
C33	O7	2.44	3.296(16)	144
C34	O3	2.38	3.222(15)	143
C34	O24#6	2.43	3.079(15)	123
C35	O24#6	2.30	3.056(16)	132
C35	O20#5	2.56	3.278(15)	129
C36	O26#3	2.56	3.516(15)	163
C55	O23#3	2.56	3.299(16)	131
C51	O16	2.57	3.277(16)	128
C51	O20	2.49	3.422(16)	156
C51	O22#3	2.47	3.287(16)	139
C52	O12#3	2.45	3.412(16)	163
C52	O16	2.47	3.199(17)	130
C53	O16	2.53	3.352(17)	140
C53	O15#6	2.56	3.414(17)	144
C54	O2w#7	2.57	3.521(18)	160
C56	O22#3	2.51	3.380(15)	146
C56	O23#3	2.54	3.261(15)	129
C71	O5	2.55	3.435(16)	148
C72	O24	2.59	3.366(16)	135
C73	O10#3	2.51	3.239(18)	130
C73	O11	2.47	3.443(17)	168
C74	O5	2.52	3.317(16)	138
C74	O1#3	2.43	3.374(16)	158
C74	O10#3	2.59	3.307(16)	129
C75	O4#3	2.55	3.436(16)	149
C76	O26#4	2.55	3.411(15)	146

Symmetry codes: *#1* −x, 2−y, 1/2 + z ; *#2* −x, 1−y, 1/2 + z; *#3* x, −1 + y, z; *#4* −1/2 + x, 3/2-y, z; *#5* 1/2−x, −1/2 + y, −1/2 + z; *#6* 1/2 + x, 3/2−y, z; *#7* 1/2−x, −1/2 + y, 1/2 + z; *#8* −x, 2−y, −1/2 + z

DABCO, under solvothermal conditions generally result in a partial reduction of V^{V}–V^{IV} and, therefore, a degree of mixed valence states in the final structures. Each decavanadate anion is surrounded by organic moieties and water molecules and shows no direct contact with the same species (Fig. 4b). It can therefore be flagged as a monomer according to the classification of the decavanadate network structures proposed by J.L. Ferreira da Silva [8]. This agrees well with the assumption that approximately spherical organic molecules, DABCO in this case, promote the monomer function of the decavanadate in the formation of organic–inorganic supramolecular assemblies [8, 10].

Regarding the organic building units in **1**, there are two distinct pairs of H_2DABCO^{2+}-$HDABCO^{+}$ and H_2DABCO^{2+}-DABCO units in the asymmetric unit (Fig. 4b). The significantly short intermolecular N···N distances—N1···N8 2.65(2) Å, N2···N7 2.67(2) Å and N4···N6 2.64(2) Å—are an indication of the presence of hydrogen atoms and hence hydrogen bonds between each pair of these DABCO molecules [22]. Each H_2DABCO^{2+}-$HDABCO^{+}$ hydrogen—bonded pair forms an isolated unit, whereas the H_2DABCO^{2+}-DABCO pairs are arranged in a fashion that leads to an infinite H-DABCO-H···DABCO···H-DABCO-H···DABCO··· hydrogen—bonded sinusoidal chain, each of which is aligned along the *c*-axis. According to the hydrogen bonding analysis results conducted using PLATON, there are both conventional and weak hydrogen bonds established between these building units as summarized in Table 4 and illustrated in Fig. 5. The large number of the otherwise weak hydrogen bonds is not common and should be noted. These weak interactions help enforce the spatial arrangement of the organic building units in the network and, therefore, impart a distinct influence on the supramolecular organization in addition to the stronger hydrogen—bonding and electrostatic interactions. The single proton attached to the decavanadate forms a classical hydrogen bond with the water oxygen atom, which acts as the hydrogen—bond acceptor (O17···O2w 2.926(13) Å, ∠O17–H···O2w 177(11)°). The

A8

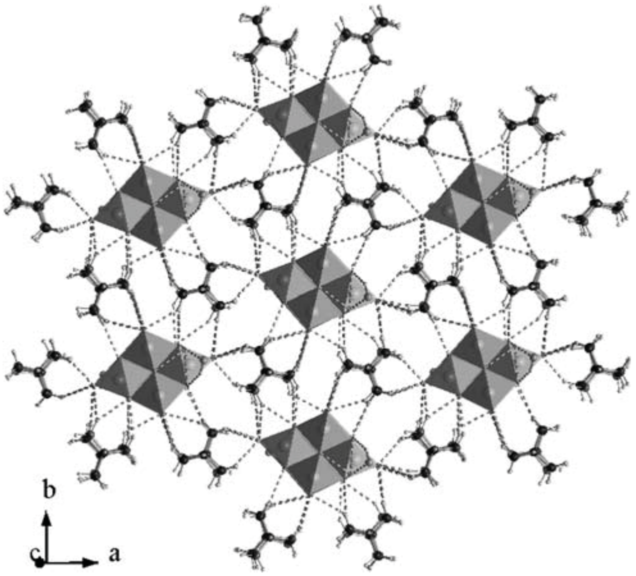

Fig. 5 The abundance of the hydrogen bonding interactions (*dotted lines*) between the supramolecular assemblies building units, viewed along the *c*-axis

formation of this hydrogen bond supports the choice of protonation site suggested by BVS calculations. The impact of the electrostatic interactions undoubtedly results in the dense network of **1**, which is characteristic of an ionic structure. Therefore, the electrostatic and hydrogen bonding interactions are synergistically responsible for the observed dense supramolecular assemblies in **1**.

4 Conclusion

Microwave heating has been successfully applied to the synthesis and growth of single crystals in a very short reaction time of a new three-dimensional hydrogen bond-assisted organic–inorganic supramolecular assembly based on decavanadate and DABCO. Single crystals suitable for complete structural characterization can be produced although twinning seems to be an inherent problem due to the fast mass transport induced by microwave heating. The nature of the crystalline product in the V_2O_5—DABCO—water system depends on the initial V_2O_5:DABCO ratio and microwave heating time; to generate single crystals of **1**, an equimolar mixture of reactants and a few hours of microwave heating is required. The single crystal experiment reveals the importance of both the abundant hydrogen bonds and the stronger electrostatic interactions in regulating the architecture of the assembly. The hydrogen bonding on the other hand is governed by the number and spatial orientation of protonation on the structural building units.

5 Supplementary Material

Crystallographic data (excluding structure factors) for structure **1** has been deposited with the Cambridge Crystallographic Data Centre (deposition numbers: CCDC 688180). Copies of this information may be obtained free of charge from The Director, CCDC, 12 Union Road, Cambridge CB2 1EZ, UK (fax: +44 1223 336033; e-mail: deposit@ccdc.cam.ac.uk).

Acknowledgments The Thailand Research Fund, the Thailand Toray Science Foundation and the Center of Excellence for Innovation in Chemistry are acknowledged for financial support. B. Yotnoi thanks to the Royal Golden Jubilee Ph.D Program and the Graduate School of Chiang Mai University for Graduate Scholarship.

References

1. D.E. Katsoulis, Chem. Rev. **98**, 359 (1998)
2. N. Mizuno, M. Misono, Chem. Rev. **98**, 199 (1998)
3. M. Aureliano, J. Inorg. Bio. **80**, 141 (2000)
4. M. Aureliano, R.M.C. Gandara, J. Inorg. Bio. **99**, 979 (2005)
5. L.J. Csányi, K. Jákya, G. Dombi, F. Evanics, G. Dezso, Z. Kóta, J. Mol. Catal. A: Chem. **195**, 101 (2003)
6. S.S. Soares, H. Martins, R.O. Duarte, J.J.G. Moura, J. Coucelo, C. Gutiérrez-Merino, M. Aureliano, J. Inorg. Bio. **101**, 80 (2007)
7. D.C. Crans, B. Baruah, N.E. Levinger, Biomed. Pharmacother. **60**, 174 (2006)
8. J.L. Ferreira da Silva, M.F. Minas da Piedade, M.T. Duarte, Inorg. Chim. Acta **356**, 222 (2003)
9. H. Kumagai, M. Arishima, S. Kitagawa, K. Ymada, S. Kawata, S. Kaizaki, Inorg. Chem. **41**, 1989 (2002)
10. I. Correia, F. Avecilla, S. Marcao, J.C. Pessoa, Inorg. Chim. Acta **357**, 4476 (2004)
11. K. Pavani, S. Upreti, A. Ramanan, J. Chem. Sci. **118**, 159 (2006)
12. D. Wang, W. Zhang, K. Gruning, D. Rehder, J. Mol. Struct. **656**, 79 (2003)
13. C.O. Kappe, Angew. Chem. Int. Ed. **43**, 6284 (2004)
14. S. Shi, J.-Y. Hwang, J. Mineral Mater. Charac. Eng. **2**, 101 (2003)
15. D.E. Clark, W.H. Sutton, Annu. Rev. Mater. Sci. **26**, 299 (1996)
16. J.H. Boosk, R.F. Cooper, S.A. Freeman, Mat. Res. Innovat. **1**, 77 (1997)
17. G.M. Sheldrick, *SHELEXS-93: A Program for Sloving Crystal Structure* (University of Goettingen, Germany, 1993)
18. G.M. Sheldrick, in *SHELEXL-97: a program for crystal structure refinement* (University of Goettingen, Germany, 1997) Release 97–2
19. A.L. Spek, *A preliminary Introduction to the PLATON Program* (Utrecht, Netherlands, 1997)
20. V.S. Urusov, I.P. Orlov, Cryst. Rep. **44**, 686 (1999)
21. I.D. Brown, *The Chemical Bond in Inorganic Chemistry: The Bond Valence Model* (Oxford University Press, Oxford, 2002)
22. T. Akutagawa, S. Takeda, T. Hasegawa, T. Nakamura, J. Am. Chem. Soc. **126**, 291 (2004)

J Chem Crystallogr (2009) 39:525–529
DOI 10.1007/s10870-009-9529-9

A9

ORIGINAL PAPER

Preparation and Characterization of Bis(μ-1,2-diaminoethane)cobalt(II) Hexavanadate: A Layered Polyoxovanadate Pillared by a Cobalt Coordination Complex

Bunlawee Yotnoi · Jumras Limtrakul ·
Timothy Prior · Apinpus Rujiwatra

Received: 7 October 2008 / Accepted: 17 February 2009 / Published online: 26 February 2009

Abstract The first example of polyoxovanadate layered framework with a cobalt coordination complex as a pillaring unit, $Co^{II}(\mu\text{-}C_2N_2H_8)_2[V^{IV}_4V^{V}_2O_{14}]$, was readily synthesized under hydrothermal conditions. The structure can be solved and refined in monoclinic $P2_1/n$ with $a = 9.143(3)$ Å, $b = 6.5034(11)$ Å, $c = 15.874(4)$ Å, $\beta = 101.90(2)$, $V = 923.6(4)$ Å^3 and $Z = 2$. The crystal structure comprises two-dimensional $\{V^{IV}_4V^{V}_2O_{14}\}^{2-}$ layers extending parallel to [101], constructed from tetrahedral $\{V^{V}O_4\}$ and square pyramidal $\{V^{IV}O_5\}$ building units. Adjacent layers are linked through the octahedral $\{Co^{II}O_2(\mu\text{-}C_2N_2H_8)_2\}$ pillars, within which the Co^{II} resides on an inversion center. The structure displays N–H···O and C–H···O hydrogen bonding between the ethylenediamine and vanadium oxide layers.

Keywords Polyoxovanadate · Cobalt · Pillaring · Ethylenediamine · Crystal structure · Hydrothermal synthesis

Introduction

Polyoxovanadate frameworks (POVs) have been capturing broad interest from materials chemists primarily because of their technological potential, e.g., as oxidative catalysts and secondary cathode materials for advanced lithium batteries [1, 2]. The inherent ability of vanadium atom to adopt various coordination geometries and oxidation states while being a good electron-acceptor and electron relay-station is also a driving force for the research in the field [3, 4]. Current interest regarding the preparation of POVs focuses on the introduction of a secondary metal, particularly a transition metal to the coordinate covalent POV frameworks. Cobalt is unique in its coordination chemistry, redox activity and potential magnetic functionality, and therefore has been one of the most studied secondary metals. Although there are earlier reports on the successful introduction of cobalt into POV frameworks (Co-POV) e.g. $[Co(2,2'\text{-bpy})_2]_2[As_8VO_{42}(H_2O)].H_2O$ [5], $[Co(en)_2(H_2O)]\{[Co(en)_2]_2As_8V_{14}O_{42}(SO_4)\}.3H_2O$ [6], $[Co(Hdpa)_2V_4O_{12}]$ [7], $Co_2(4,4'\text{-bipy})_2(V_4O_{12})$ [8] and $\{[H_2(en)]Co(ox)(V_4O_{12})\}_n$ [9], none of these are the Co-POV structures in which the cobalt present as a pillaring unit. Examples of POV frameworks where the secondary metal present acts as a pillar motif between POV sheets are rare, and limited to $(C_2N_2H_8)_2Zn[V_6O_{14}]$, $(C_2N_2H_8)_2Cu[V_6O_{14}]$, $[Ni(C_2N_2H_8)_2]_{0.5}[V_3O_7]$ and $[Ni(en\text{-}Me)_2]_{0.5}[H_2enMe]_{0.5}[V_6O_{14}]$ [10, 11]. Here, we report the preparation and crystal structure of $Co^{II}(\mu\text{-}C_2N_2H_8)_2[V^{IV}_4V^{V}_2O_{14}]$, which is the first example of a layered POV pillared by cobalt.

Experimental

Crystals of $Co^{II}(\mu\text{-}C_2N_2H_8)_2[V^{IV}_4V^{V}_2O_{14}]$ (**I**) were readily prepared from a reaction between $Co(NO_3)_2 \cdot 6H_2O$ (98% Aldrich, 0.1006 g), V_2O_5 (99% Fluka, 0.2519 g) and ethylenediamine (99% Fluka, 0.0719 g) in deionized water (2.80 cm^3) using a 17 cm^3 Teflon container. The reaction

B. Yotnoi · A. Rujiwatra (✉)
Inorganic Materials Research Unit, Department of Chemistry,
Faculty of Science, Chiang Mai University, Chiang Mai 50200,
Thailand
e-mail: apinpus@chiangmai.ac.th

J. Limtrakul
Department of Chemistry, Faculty of Science,
Kasetsart University, Bangkok 10900, Thailand

T. Prior
Department of Chemistry, University of Hull,
Kingston upon Hull HU6 7RX, UK

A10

was conducted under autogenous pressure at 473 K for 60 h before being cooled down to room temperature using a rather rapid rate of 30 K h^{-1}. Black crystals of **I** were then separated from the supernatant solution by filtration, washed with deionized water and dried in air. The elemental composition in **I** was determined using the energy dispersive X-ray spectroscopic (EDS) microanalyzer present on the scanning electron microscope (FESEM, JEOL JSM-6335F) and a Perkin Elmer Series II 2400 CHN/S analyzer. Infrared spectra of also the ground crystals were collected on a Bruker Tensor 27 FT-IR instrument (4,000–400 cm^{-1}, resolution 0.5 cm^{-1}) using a KBr (BDH 98.5%) pellet. The X-ray powder diffraction (XRD) pattern was collected using a Bruker D8 Advance diffractometer, operating with a Ni filtered Cu K_α radiation (λ = 1.5405 Å, 48 kV and 30 mA).

In order to determine the crystal structure of **I**, a full set of intensity data was collected on a single crystal of size 0.20 × 0.04 × 0.04 mm^3 at 150(2) K using a Stoe IPDS2 image plate diffractometer operating with Mo Kα radiation, employing a single ω-scan. The crystal was cooled using an Oxford Instruments nitrogen gas cryostream. The collected data were analytically corrected for absorption using the Tompa method [12]. The structure was then solved by direct methods implemented within SHELXS-97 [13] and full-matrix least squares refinement carried out within SHELXL-97 [14] via the WinGX [15] program interface. All non-hydrogen atoms were located from direct and difference Fourier maps and refined anisotropically. The hydrogen atoms in the ethylenediamine were apparent from final difference Fourier maps, and were then placed and refined using a riding model with the following bond lengths: C–H 0.99(3) Å; N–H 0.92(3) Å. Details of the data collection and structure refinements are summarized in Table 1.

Table 1 Crystallographic data for structural solution and refinement of **I**

CCDC no.	704646
Formula	$Co(C_2N_2H_8)_2[V_4^{IV}\ V_2^{V}O_{14}]$
Formula weight	708.78
Crystal size/mm	0.20 × 0.04 × 0.04
Crystal system	Monoclinic
Space group	*P2₁/n*
a (Å)	9.143(3)
b (Å)	6.5034(11)
c (Å)	15.874(4)
β (°)	101.90(2)
V_{cell} (Å^3)	923.6(4)
Z	2
ρ_{calc} (g cm^{-3})	2.549
T (K)	150(2)
Radiation (λ/Å)	Mo K_α(0.71069)
μ (mm^{-1})	3.854
θ_{min}, θ_{max}	2.85, 26.00
Unique data	1,799
Observed data	1,071
Parameters no.	134
Restrains no.	4
Goodness of fit	0.840
R, Rw (all data)	0.0853, 0.0730
R, Rw (I > 2σ(I))	0.0399, 0.0652

CCDC 704646 contains the supplementary crystallographic data for this paper. These data can be obtained free of charge by e-mailing to data_request@ccdc.cam.ac.uk, or by contacting The Cambridge Crystallographic Data Centre 12 Union Road Cambridge CB2 1EZ, UK, fax: +44-1223-336033

Results and Discussion

The crystal structure of $Co^{II}(\mu\text{-}C_2N_2H_8)_2[V_4^{IV}V_2^{V}O_{14}]$ (**I**) was successfully solved and refined in the monoclinic space group *P2₁/n* with the final refined cell parameters a = 9.143(3) Å, b = 6.5034(11) Å, c = 15.874(4) Å, β = 101.90(2)° and V = 923.6(4) Å^3. The ORTEP plot of the extended asymmetric unit showing the coordination environments of the structural building motifs and atomic numbering scheme is shown in Fig. 1. The atomic coordinates and equivalent isotropic displacement parameters are listed in Table 2. There are three crystallographically distinct sites of vanadium. The bond valence calculations based on a single point energy model [16], and refined bond distances listed in Table 3 suggest the presence of both pentavalent vanadium (V_1) and tetravalent vanadium (V_2, V_3). Although the starting vanadium source is V_2O_5, the mild reducing power of the organic component results in the mixed V^{IV}/V^{V} structure. The tetravalent V_2 and V_3 are characterized by square pyramidal geometry, $\{V^{IV}O_5\}_{sq}$, of 4 + 1 type, each of which shows four long equatorial bonds—V_2–O_2, V_2–O_3, V_2–O_6, V_3–O_2, V_3–O_3, V_3–O_5 and V_3–O_6 in range 1.894(4)–2.017(4) Å with an average of 1.958(4) Å and one short vanadyl bond—$V_2 = O_4$ (1.609(5) Å) and $V_3 = O_7$ (1.616(5) Å). The pentavalent V_1 on the other hand shows a 3 + 1 tetrahedral coordination, $\{V^{V}O_4\}_{tet}$, of which the bond lengths of the bridging V_1–O_2 (1.821(4) Å), V_1–O_5 (1.695(4) Å) and V_1–O_6 (1.792(4) Å) bonds are longer than the terminal V_1–O_1 (1.599(5) Å) bond. The distortion of the $\{V^{V}O_4\}_{tet}$ from the regular tetrahedron is apparent. The interatomic distances involving with the triply bridging oxygen, i.e. μ_3–O_2 and μ_3–O_6, are significantly longer than that of the doubly bridging oxygen, i.e. μ_2–O_5. The correlation between the refined bond distances and their corresponding polyhedral configurations agree well with the previously

A11

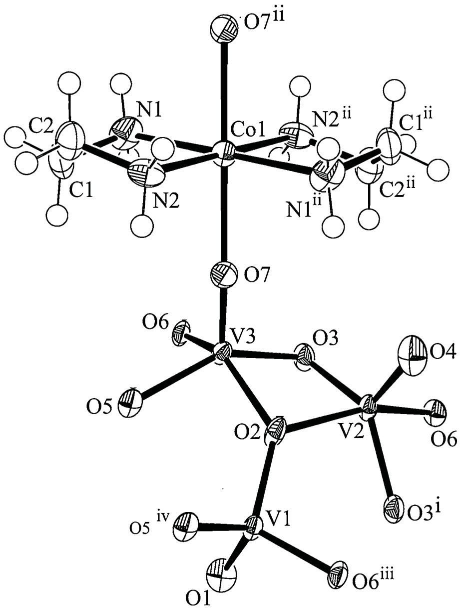

Fig 1 An ORTEP view of the extended asymmetric unit of I drawn at 80% probability level with hydrogen atoms omitted for clarity. [Symmetry codes: (i) $-x, -y + 2, -z$; (ii) $x, y + 1, z$; (iii) $-x + 1/2, y + 1/2, -z + 1/2$; (iv) $-x + 1, -y + 1, -z$]

Table 2 Atomic coordinates and equivalent isotropic displacement parameters of non-hydrogen atoms

	x	*y*	*z*	*Ueq*
V_1	0.04285(11)	1.21858(15)	0.09298(6)	0.0112(2)
V_2	0.32600(11)	1.00000(15)	0.23310(6)	0.0120(2)
V_3	0.19319(11)	0.71902(15)	0.10076(6)	0.0116(2)
O_1	−0.1016(5)	1.1633(6)	0.1306(3)	0.0195(10)
O_2	0.1848(5)	1.0192(6)	0.1188(2)	0.0147(9)
O_3	0.2778(4)	0.7166(6)	0.2232(3)	0.0149(9)
O_4	0.4825(5)	1.0572(6)	0.2077(3)	0.0236(11)
O_5	0.0077(5)	0.7489(5)	0.0151(2)	0.0144(9)
O_6	0.1161(4)	0.4589(6)	0.1384(2)	0.0133(9)
O_7	0.3237(5)	0.6607(6)	0.0501(3)	0.0184(10)
Co_1	0.50000	0.50000	0.00000	0.0140(3)
N_1	0.3691(6)	0.2363(8)	−0.0417(3)	0.0228(13)
N_2	0.3993(6)	0.6049(8)	−0.1210(4)	0.0189(12)
C_1	0.2589(7)	0.2940(11)	−0.1201(4)	0.0239(16)
C_2	0.3322(8)	0.4276(10)	−0.1741(4)	0.0242(17)

reported POV layer frameworks of the same composition and registry, e.g. $[V_6O_{14}](C_4H_{14}N_2)$, $[V_6O_{14}](C_5H_{16}N_2)$, $(C_2N_2H_8)_2Zn[V_6O_{14}]$ and $(C_2N_2H_8)_2Cu[V_6O_{14}]$ [10, 17].

Table 3 Selected bond distances for **I**

V_1–O_1	1.599(5)	V_3–O_5	1.953(4)
V_1–O_5^I	1.695(4)	V_3–O_6	1.972(4)
V_1–O_6^{II}	1.792(4)	V_3–O_2	1.976(4)
V_1–O_2	1.821(4)	Co_1–O_7	2.202(5)
V_2–O_4	1.609(5)	Co_1–N_2^{IV}	2.067(5)
V_2–O_3	1.894(4)	Co_1–N_2	2.067(5)
V_2–O_3^{III}	1.908(4)	Co_1–N_1	2.118(5)
V_2–O_2	2.002(4)	Co_1–N_1^{IV}	2.118(5)
V_2–O_6^{III}	2.017(4)	N_1–C_1	1.479(8)
V_3–O_7	1.616(5)	N_2–C_2	1.484(8)
V_3–O_3	1.938(4)	C_1–C_2	1.475(10)

Symmetry codes: (i) $-x, -y + 2, -z$; (ii) $x, y + 1, z$; (iii) $-x + 1/2, y + 1/2, -z + 1/2$; (iv) $-x + 1, -y + 1, -z$

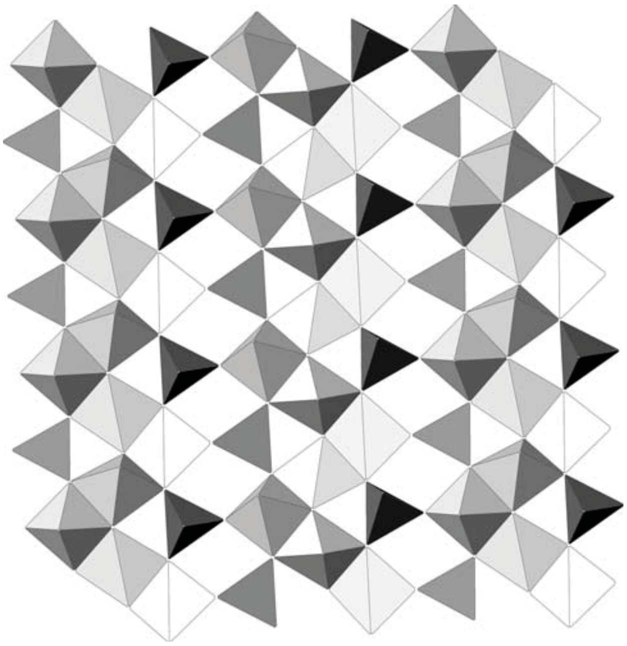

Fig 2 A polyhedral view of the ({UuDd}:T.) β-POV layer in **I**

Two adjacent $\{V^{IV}O_5\}_{sq}$ units share edges in a *trans* conformation to form a larger binuclear $\{V_2^{IV}O_8\}$ unit, which is then fused through *cis* edge sharing to the neighboring binuclear units to generate the {UuDd} or {Z} chain with a zigzag configuration as shown in Fig. 2. Each chain is connected to the adjacent chains by the $\{V^VO_4\}_{tet}$, each of which share two basal corners with one chain and the other basal corner with the other chain. This results in a mixed valence $[V_4^{IV}O_{10}V_2^VO_4]^{2-}$ anionic layer of ({UuDd}: T.)β type in SP + T class and Z-T subclass [18]. These anionic POV layers extend parallel to the [101], and are linked further by the octahedral $\{Co^{II}O_2\,(C_2N_2H_8)_2\}$ pillars via the two *trans* apical O_7 atoms of the $\{V^{IV}O_5\}_{sq}$ from two adjacent layers to generate a three-dimensional pillared Co-POV structure (Fig. 3), which is isostructural with the zinc, copper and nickel analogues, $(C_2N_2H_8)_2Zn[V_6O_{14}]$, $(C_2N_2H_8)_2Cu[V_6O_{14}]$ and $[Ni(C_3N_2H_{11})_2]_{0.5}[C_3N_2H_{13}]_{0.5}[V_6O_{14}]$ [10, 11]. This implies the template function of the ethylenediamine and therefore the feasibility in crystal engineering of other analogous pillared structures. The pseudo-octahedral coordination of the cobalt is completed

A12

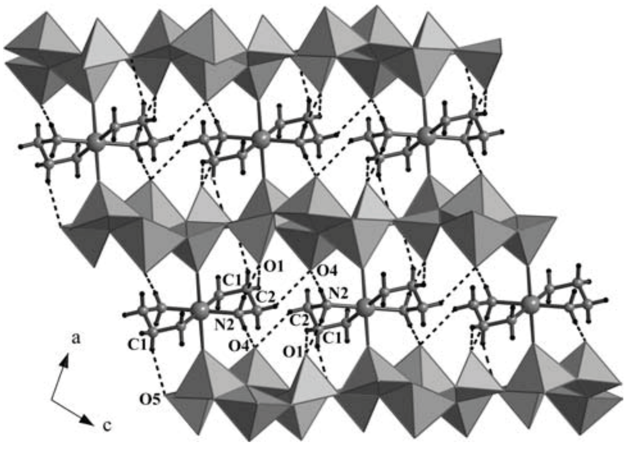

Fig 3 View of the three-dimensional structure of **I** with hydrogen bonds shown in *dotted lines*

by four nitrogen atoms from two *trans* ethylenediamine ligands, locating about the inversion center at the cobalt atom. The bond valence calculations suggested the divalent state of the cobalt and therefore a dipositively charged $\{Co^{II}O_2(C_2N_2H_8)_2\}$ pillar, which consequently balances the negatively charged POV layer. **I** is similar in some respects to the framework $[\{Co(pyz)\}(V_2O_5)_2]$, pyz = pyrazine [19], which has been reported recently. In **I** the layers are linked by discrete $Co(en)_2^{2+}$ units, but in $[\{Co(pyz)\}(V_2O_5)_2]$ layers are linked by a series of 1-D chains of formulation $Co(pyz)^2$. However, a different POV layer of type 2({UUDD}) is present within $[\{Co(pyz)\}(V_2O_5)_2]$.

The analysis of hydrogen bonding interactions as listed in Table 4 suggests the spatial arrangement of the ethylenediamine to be partially imparted by the hydrogen bonds established between both the polar nitrogen atoms and the methylene carbon atoms of the organic molecule, and the vanadyl oxygen atoms of the POV layer, i.e. N–H···O and C–H···O. Although the established C–H···O hydrogen bonds are very weak [20], they may play a part in synergistic with the octahedral coordination geometry of the Co^{II} ion, in regulating the spatial arrangement of the ethylenediamine in relative to the POV layer. It is apparent from Fig. 3 that the ethylenediamines acting as a bidentate ligand are arranged roughly in a plane parallel to the POV layers, which is also the case for the analogous $(C_2N_2H_8)_2Zn[V_6O_{14}]$ and $(C_2N_2H_8)_2Cu[V_6O_{14}]$ structures [17].

Table 4 Hydrogen bonding geometry for **I**

D–H···A	D–H	H···A	D···A	D–H···A
N_2–$H_2C\cdots O_1^{I}$	0.92	2.21	3.088(7)	159
N_2–$H_2D\cdots O_4^{V}$	0.92	2.12	2.916(7)	144
C_1–$H_1A\cdots O_1^{VI}$	0.99	2.47	3.293(8)	140
C_1–$H_1B\cdots O_5^{VI}$	0.99	2.51	3.237(9)	130
C_2–$H_2A\cdots O_4^{VII}$	0.99	2.54	3.359(8)	140

Symmetry codes: (i) $-x, -y + 2, -z$; (v) $-x + 1, -y + 2, -z$; (vi) $-x, -y + 1, -z$; (vii) $x - 1/2, -y + 3/2, z - 1/2$

Elemental analysis of ground crystal using an energy dispersive X-ray spectroscopic (EDS) microanalyzer confirms the crystallographically observed ratio of 1:6 for Co:V. CHNS analysis data of bulk samples fit rather poorly to the crystallographically observed formulation. [found—C 46.61%, N 39.97%, H 13.42%; calculated—C 50.04%, N 39.45%, H 10.50%]. The data suggest impurities are present, possibly with coordinated water. However, the X-ray powder diffraction data show that the pillared phase is the dominant crystalline component present in the bulk. The FT-IR spectrum collected on the ground crystals reveals the existence of the major functional groups of the ethylenediamine and the ligated atoms to the cobalt; 3452vs, 3015vs (ν(N–H; NH_2)); 1630s (δ(N–H)); 1463m (δ(C–H; CH_2)); 1055m (ν(C–N)); 973s (ν(V–O_t)); 740s (ν(V–O_b)); 673m (ν(Co–N)); 465m (ν(Co–O)). The broadening effect is also observed in the spectrum which is consistent with the presence of the hydrogen bonds.

In conclusion, a new pillared POV layer structure of the Co-POV system has been prepared and fully characterized. This expands a series of the pillared POV layer structures to include Zn-POV, Cu-POV, Ni-POV and Co-POV, which in turn suggest the template function of the ethylenediamine and therefore the feasibility in extending this structural series to other secondary metals with possibly better potential functions. Work to prepare a pure sample of **I** is underway with a view to examining the magnetic behavior of the pillared framework.

Acknowledgments The Thailand Research Fund, the Commission for Higher Education, the Center of Excellence for Innovation in Chemistry, and the Thailand Toray Science Foundation are acknowledged for financial support. B. Yotnoi thanks the Royal Golden Jubilee Ph.D. Program and the Graduate School of Chiang Mai University for Graduate Scholarship.

References

1. Hagrman PJ, Finn RC, Zubieta J (2001) Solid State Sci 3:745
2. Davi RN, Zubieta J (2003) Inorg Chim Acta 343:313
3. Li GH, Shi Z, Xu YH, Feng SH (2003) Inorg Chem 42:1170
4. Coronado E, Gomez-Garcya CL (1999) Chem Soc 121:11459
5. Wang CM, Zeng QX, Zhang J, Yang GY (2005) J Clust Sci 16:65
6. Zhou G, Xu Y, Guo C, Zheng X (2007) Inorg Chem Commun 10:849
7. LaDuca RL, Rarig RS, Zubieta J (2001) Inorg Chem 40:607
8. Zheng LM, Wang X, Wang Y, Jacobson AJ (2001) J Mater Chem 11:1100
9. Pan CL, Xu JQ, Wang KX, Cui XB, Ye L, Lu ZL, Chu DQ, Wang TG (2003) Inorg Chem Commun 6:370
10. Zhang Y, DeBord JRD, O'Connor CJ, Haushalter RC, Clearfield A, Zubieta J (1996) Angew Chem Int Ed Engl 35:989
11. Shi Z, Zhang L, Zhu G, Yang G, Hua J, Ding H, Feng S (1999) Chem Mater 11:3565

A13

12. de Meulener J, Tompa H (1965) Acta Crystallogr 19:1014
13. Sheldrick GM (1997) SHELXS-97, program for solving crystal structure. University of Gottingen, Germany
14. Sheldrick GM (1997) SHELXL-97, program for crystal structure refinement. University of Gottingen, Germany
15. Farrugia LJ (1999) J Appl Crystallogr 32:837
16. Urusov VS, Orlov IP (1999) Crystallogr Rep 44:686
17. Settheeworrarit T, Prior TJ, Meansiri S, Limtrakul J, Rujiwatra A (2008) J Inorg Organomet Polym 18:253
18. Zavalij PY, Whittingham MS (1999) Acta Crystallogr B55:627
19. Khan MI, Yohannes E, Golub VO, O'Connor CJ, Doedens RJ (2007) Chem Mater 19:1890
20. Desiraju G (2003) J Mol Struct 656:5

Acta Crystallographica Section E
Structure Reports
Online

ISSN 1600-5368

(1-Butyl-1,4-diazabicyclo[2.2.2]octon-1-ium-κN^4)trichloridocobalt(II)

Sanchai Luachan,[a] Bunlawee Yotnoi,[a] Timothy J. Prior[b] and Apinpus Rujiwatra[a]*

[a]Department of Chemistry, Faculty of Science, Chiang Mai University, Chiang Mai 50200, Thailand, and [b]Department of Chemistry, University of Hull, Kingston upon Hull HU6 7RX, England
Correspondence e-mail: apinpus@chiangmai.ac.th

Received 11 February 2009; accepted 19 February 2009

Key indicators: single-crystal synchrotron study; T = 120 K; mean σ(C–C) = 0.007 Å; R factor = 0.045; wR factor = 0.098; data-to-parameter ratio = 30.2.

The title compound, $[Co(C_{10}H_{21}N_2)Cl_3]$, was obtained as the by-product of the attempted synthesis of a cobalt sulfate framework using 1,4-diazabicyclo[2.2.2]octane as an organic template. The asymmetric unit comprises two distinct molecules, and in each, the cobalt(II) ions are tetrahedrally coordinated by three chloride anions and one 1-butyldiazabicyclo[2.2.2]octan-1-ium cation. The organic ligands are generated *in situ*, and exhibit two forms differentiated by the eclipsed and staggered conformations of the butyl groups. These molecules interact by way of C—H⋯Cl hydrogen bonds, forming a three-dimensional hydrogen-bonding array.

Related literature

Examples of closely related structures are *N*-methyl-1,4-diazabicyclo(2.2.2) octonium trichloro-aqua-nickel(II) (Ross & Stucky, 1969) and *N*,*N*′-dimethyl-1,4-diazaniabicyclo[2.2.2]-octane tetrachlorocobaltate $(C_8H_{18}N_2)[CoCl_4]$ (Qu & Sun, 2005). The organic cation in both structures do not coordinate to the cobalt ion but, in each case, the C—H⋯Cl hydrogen-bonding interactions are similar to those in the title compound. For hydrogen bonding in related structures, see: Bremner & Harrison (2003).

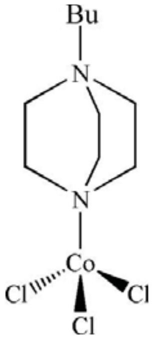

Experimental

Crystal data

$[Co(C_{10}H_{21}N_2)Cl_3]$
M_r = 334.57
Monoclinic, $P2_1$
a = 8.379 (2) Å
b = 12.1090 (13) Å
c = 14.711 (4) Å
β = 91.683 (4)°
V = 1492.0 (6) Å^3
Z = 4
Synchrotron radiation
λ = 0.69430 Å
μ = 1.67 mm^{-1}
T = 120 K
0.12 × 0.02 × 0.02 mm

Data collection

Bruker D8 with APEXII detector diffractometer
Absorption correction: multi-scan (TWINABS; Bruker, 2004)
T_{min} = 0.597, T_{max} = 0.746 (expected range = 0.774–0.967)
12848 measured reflections
8831 independent reflections
7018 reflections with $I > 2\sigma(I)$
R_{int} = 0.054

Refinement

$R[F^2 > 2\sigma(F^2)]$ = 0.045
$wR(F^2)$ = 0.098
S = 1.04
8831 reflections
292 parameters
1 restraint
H-atom parameters constrained
$\Delta\rho_{max}$ = 0.65 e Å^{-3}
$\Delta\rho_{min}$ = −0.44 e Å^{-3}
Absolute structure: Flack (1983), 3980 Friedel pairs
Flack parameter: 0.064 (17)

Table 1
Hydrogen-bond geometry (Å, °).

D—H⋯A	D—H	H⋯A	D⋯A	D—H⋯A
C2—H2B⋯Cl6^{i}	0.99	2.66	3.567 (5)	153
C4—H4A⋯Cl1^{ii}	0.99	2.66	3.511 (5)	145
C6—H6B⋯Cl3^{ii}	0.99	2.69	3.606 (5)	154
C7—H7B⋯Cl3^{iii}	0.99	2.80	3.729 (5)	157
C12—H12B⋯Cl5^{iv}	0.99	2.62	3.485 (4)	146
C14—H14A⋯Cl6^{iv}	0.99	2.75	3.567 (5)	140
C16—H16A⋯Cl1^{v}	0.99	2.60	3.548 (4)	161
C16—H16B⋯Cl5^{v}	0.99	2.81	3.739 (4)	156

Symmetry codes: (i) $x-1, y, z-1$; (ii) $-x, y-\frac{1}{2}, -z+1$; (iii) $x-1, y, z$; (iv) $-x+2, y-\frac{1}{2}, -z+2$; (v) $x+1, y, z$.

Data collection: *APEX2* (Bruker, 2007); cell refinement: *APEX2*; data reduction: *TWINABS* (Bruker, 2004); program(s) used to solve structure: *SHELXS86* (Sheldrick, 2008); program(s) used to refine structure: *SHELXL97* (Sheldrick, 2008); molecular graphics: *DIAMOND* (Brandenburg & Putz, 2005); software used to prepare material for publication: *PLATON* (Spek, 2009).

The authors thank the Thailand Research Fund, Center for Innovation in Chemistry and Thailand Toray Science Foundation for financial support. BY thanks the Royal Golden Jubilee PhD program and the Graduate School of Chiang Mai University for a Graduate Scholarship.

Supplementary data and figures for this paper are available from the IUCr electronic archives (Reference: LH2775).

References

Brandenburg, K. & Putz, H. (2005). *DIAMOND*. Crystal Impact GbR, Bonn, Germany.
Bremner, C. A. & Harrison, W. T. A. (2003). *Acta Cryst.* E**59**, m425–m426.
Bruker (2004). *TWINABS*. Bruker AXS Inc., Madison, Wisconsin, USA.
Bruker (2007). *APEX2*. Bruker AXS Inc., Madison, Wisconsin, USA.
Flack, H. D. (1983). *Acta Cryst.* A**39**, 876–881.

Acta Cryst. (2009). E**65**, m321–m322 doi:10.1107/S1600536809005893 Luachan *et al.* **m321**

Qu, Y. & Sun, X.-M. (2005). *Acta Cryst.* E**61**, m2121–m2123.
Ross, F. K. & Stucky, G. D. (1969). *Inorg. Chem.* **8**, 2734–2740.
Sheldrick, G. M. (2008). *Acta Cryst.* A**64**, 112–122.
Spek, A. L. (2009). *Acta Cryst.* D**65**, 148–155.

m322 Luachan *et al.* • [Co($C_{10}H_{21}N_2$)Cl_3] *Acta Cryst.* (2009). E**65**, m321–m322

A16

Acta Cryst. (2009). E**65**, m321-m322   [**doi:10.1107/S1600536809005893**]

(1-Butyl-1,4-diazabicyclo[2.2.2]octon-1-ium-κN^4)trichloridocobalt(II)

S. Luachan, B. Yotnoi, T. J. Prior and **A. Rujiwatra**

Comment

The crystals of Co($C_{10}H_{21}N_2$)Cl_3 (**I**) were unintentionally obtained as a by-product from the hydrothermal reaction between cobalt(II) sulfate heptahydrate and 1,4-diazabicyclo[2.2.2]octane in a water/butan-1-ol mixture. The *N*-butyl-1,4-diazabicyclo[2.2.2]octanium ligand was presumably generated *in situ* under acidic conditions. The structure of I is built up from two distinct [Co($C_{10}H_{21}N_2$)Cl_3] molecules as shown in Fig. 1. They are different in the spatial orientation of the butyl group of the *N*-butyl-1,4-diazabicyclo[2.2.2]octanium ligand, one of which is in the eclipsed conformation (**A**) and the other is in the staggered conformation (**B**). The **A** molecules are connected by the C—H···Cl hydrogen bonding interactions to form a two-dimensional **A** sheet in the *ab* plane (Fig. 2), whereas the **B** molecules form the **B** sheet also in the*ab* plane using similar C—H···Cl hydrogen bonding interactions (Fig. 3). The **A** and **B** sheets are then regularly alternated in the **ABAB** fashion, and linked by way of also the C—H···Cl hydrogen bonding interactions along *c* to give the infinite three-dimensional hydrogen bonding array (Fig. 4).

The hydrogen bond geometries found in **I** (H···Cl, 2.62–2.81 Å; C···Cl, 3.485 (4)–3.739 (4) Å; C—H···Cl, 140.00–164.00°) are well comparable to those found in related structures, *e.g.* ($C_6H_{14}N_2$)[$CoCl_4$] (Bremner & Harrison, 2003) and ($C_8H_{18}N_2$)[$CoCl_4$] (Qu & Sun, 2005).

Experimental

Crystals of **I** were obtained as a by-product from the hydrothermal reaction of cobalt(II) sulfate heptahydrate, 1,4-diazabicyclo[2.2.2]octane and hydrochloric acid in a water/butan-1-ol mixture at 453 K for 120 h.

Refinement

H atoms were placed in calcluated positions with C-H = 0.99Å or 0.98Å for methyl H atoms and were included in the refinement in a riding-model approximation with U_{iso}(H) = 1.2U_{eq}(C) or 1.5U_{eq}(C) for methyl H atoms.

The examined crystal was found to be twinned, composing of two crystal components which were miss-set by about two degrees. The crystal was therefore treated as a twin and the two components integrated separately using the same unit cell. Both components were used for the structure refinement and the twin fraction was found to be 0.698:0.302 (1).

Three alerts from checkCIF:

PLAT220_ALERT_2_C

PLAT222_ALERT_2_C

A17

The rather weak van der Waals interactions involving the *n*-butyl chains mean there is considerable freedom for these carbon and hydrogen atoms to vibrate. The slightly enlarged displacement parameters observed are entirely expected on chemical grounds.

PLAT341_ALERT_3_C

The calculated estimated standard uncertainties associated with the unit-cell parameters are faithfully reproduced from the Bruker APEXII suite (Bruker, 2004). All observed data were used in their calculation. These give rise to moderate precision in the C—C bonds. To some extent this is a consequence of the integration procedure which uses two twin components - deconvolution of the low angle components is problematic as the two componenets are miss-set by approximately 2°.

Figures

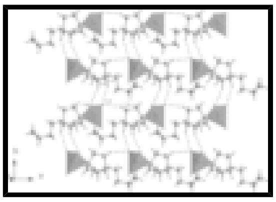

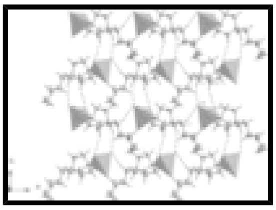

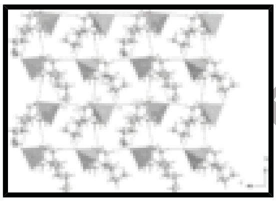

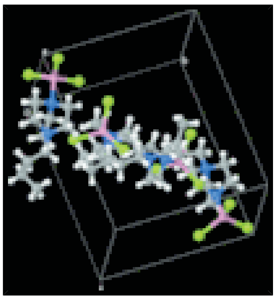

View of the title compound with the atom numbering scheme. Displacement ellipsoids for non-H atoms are drawn at the 70% probability level.

View of the **A** sheet along the *ab* plane with the hydrogen bonding atoms indicated.

View of the **B** sheet along the *ab* plane with the hydrogen bonding atoms indicated.

The packing of **A** and **B** sheets along *c* in **ABAB** fashion.

A18

(1-Butyl-1,4-diazabicyclo[2.2.2]octon-1-ium-κN^4)trichloridocobalt(II)

Crystal data

$[Co(C_{10}H_{21}N_2)Cl_3]$

M_r = 334.57

Monoclinic, $P2_1$

Hall symbol: P 2yb

a = 8.379 (2) Å

b = 12.1090 (13) Å

c = 14.711 (4) Å

β = 91.683 (4)°

V = 1492.0 (6) Å^3

Z = 4

F_{000} = 692

D_x = 1.490 Mg m^{-3}

Synchrotron radiation
λ = 0.69430 Å

Cell parameters from 12848 reflections

θ = 1.4–30.7°

μ = 1.67 mm^{-1}

T = 120 K

Needle, blue

0.12 × 0.02 × 0.02 mm

Data collection

Bruker D8 with APEXII detector diffractometer

Radiation source: Daresbury SRS, UK

Monochromator: silicon 111

T = 120 K

ω scans

Absorption correction: multi-scan (TWINABS; Bruker, 2004)

T_{min} = 0.597, T_{max} = 0.746

12848 measured reflections

8831 independent reflections

7018 reflections with $I > 2\sigma(I)$

R_{int} = 0.054

θ_{max} = 30.7°

θ_{min} = 1.4°

$h = -12 \rightarrow 12$

$k = -17 \rightarrow 17$

$l = -20 \rightarrow 20$

Refinement

Refinement on F^2

Least-squares matrix: full

$R[F^2 > 2\sigma(F^2)]$ = 0.045

$wR(F^2)$ = 0.098

S = 1.04

8831 reflections

292 parameters

1 restraint

Primary atom site location: structure-invariant direct methods

Secondary atom site location: difference Fourier map

Hydrogen site location: inferred from neighbouring sites

H-atom parameters constrained

$w = 1/[\sigma^2(F_o^2) + (0.0352P)^2 + 0.2945P]$
where $P = (F_o^2 + 2F_c^2)/3$

$(\Delta/\sigma)_{max}$ = 0.001

$\Delta\rho_{max}$ = 0.65 e Å^{-3}

$\Delta\rho_{min}$ = −0.43 e Å^{-3}

Extinction correction: none

Absolute structure: Flack (1983), 3980 Friedel pairs

Flack parameter: 0.064 (17)

Special details

Geometry. All e.s.d.'s (except the e.s.d. in the dihedral angle between two l.s. planes) are estimated using the full covariance matrix. The cell e.s.d.'s are taken into account individually in the estimation of e.s.d.'s in distances, angles and torsion angles; correlations between e.s.d.'s in cell parameters are only used when they are defined by crystal symmetry. An approximate (isotropic) treatment of cell e.s.d.'s is used for estimating e.s.d.'s involving l.s. planes.

Refinement. Refinement of F^2 against ALL reflections. The weighted R-factor wR and goodness of fit S are based on F^2, conventional R-factors R are based on F, with F set to zero for negative F^2. The threshold expression of $F^2 > \sigma(F^2)$ is used only for calculating R-factors(gt) *etc*. and is not relevant to the choice of reflections for refinement. R-factors based on F^2 are statistically about twice as large as those based on F, and R- factors based on ALL data will be even larger.

Fractional atomic coordinates and isotropic or equivalent isotropic displacement parameters (Å^2)

	x	y	z	$U_{\rm iso}$*/$U_{\rm eq}$
Co1	0.17969 (6)	0.70552 (4)	0.56075 (3)	0.02973 (12)
Cl1	0.08844 (13)	0.78922 (10)	0.68543 (6)	0.0382 (2)
Cl2	0.28560 (14)	0.53800 (9)	0.58911 (8)	0.0416 (2)
Cl3	0.32696 (13)	0.81305 (9)	0.47062 (7)	0.0373 (2)
N1	−0.0308 (4)	0.6782 (3)	0.48346 (19)	0.0264 (7)
N2	−0.2901 (4)	0.6376 (3)	0.3900 (2)	0.0278 (7)
C1	−0.1094 (5)	0.7827 (4)	0.4539 (3)	0.0304 (8)
H1A	−0.0310	0.8306	0.4240	0.037*
H1B	−0.1485	0.8224	0.5077	0.037*
C2	−0.2502 (5)	0.7587 (3)	0.3875 (3)	0.0296 (9)
H2A	−0.3443	0.8026	0.4047	0.036*
H2B	−0.2216	0.7801	0.3251	0.036*
C3	0.0056 (5)	0.6132 (4)	0.4005 (3)	0.0327 (9)
H3A	0.0741	0.5495	0.4175	0.039*
H3B	0.0647	0.6601	0.3578	0.039*
C4	−0.1487 (5)	0.5719 (4)	0.3539 (3)	0.0319 (9)
H4A	−0.1630	0.4923	0.3665	0.038*
H4B	−0.1430	0.5818	0.2872	0.038*
C5	−0.1470 (5)	0.6141 (4)	0.5373 (3)	0.0318 (8)
H5A	−0.1588	0.6499	0.5972	0.038*
H5B	−0.1048	0.5386	0.5480	0.038*
C6	−0.3093 (5)	0.6065 (4)	0.4892 (2)	0.0315 (8)
H6A	−0.3853	0.6575	0.5179	0.038*
H6B	−0.3516	0.5305	0.4937	0.038*
C7	−0.4381 (6)	0.6160 (4)	0.3329 (3)	0.0351 (9)
H7A	−0.4196	0.6415	0.2701	0.042*
H7B	−0.5264	0.6607	0.3569	0.042*
C8	−0.4898 (7)	0.4966 (4)	0.3294 (3)	0.0477 (13)
H8A	−0.5210	0.4732	0.3909	0.057*
H8B	−0.3982	0.4504	0.3118	0.057*
C9	−0.6289 (7)	0.4765 (5)	0.2626 (3)	0.0541 (15)
H9A	−0.7187	0.5257	0.2779	0.065*
H9B	−0.5958	0.4951	0.2004	0.065*

C10	−0.6843 (9)	0.3581 (7)	0.2648 (4)	0.086 (3)
H10A	−0.5968	0.3094	0.2473	0.129*
H10B	−0.7752	0.3484	0.2221	0.129*
H10C	−0.7167	0.3393	0.3264	0.129*
Co2	0.86290 (6)	0.69012 (4)	1.06702 (3)	0.02719 (12)
Cl4	0.74916 (13)	0.52684 (9)	1.09830 (7)	0.0360 (2)
Cl5	0.70380 (13)	0.79352 (9)	0.97538 (7)	0.0361 (2)
Cl6	0.97391 (13)	0.78267 (9)	1.18605 (6)	0.0331 (2)
N3	1.0632 (4)	0.6586 (3)	0.98991 (19)	0.0256 (7)
N4	1.3114 (4)	0.6133 (3)	0.8981 (2)	0.0266 (7)
C11	1.1771 (5)	0.5881 (4)	1.0443 (2)	0.0335 (9)
H11A	1.1303	0.5138	1.0523	0.040*
H11B	1.1955	0.6211	1.1052	0.040*
C12	1.3367 (5)	0.5778 (3)	0.9963 (2)	0.0290 (8)
H12A	1.4181	0.6254	1.0268	0.035*
H12B	1.3748	0.5005	0.9990	0.035*
C13	1.0170 (5)	0.5989 (4)	0.9044 (3)	0.0323 (9)
H13A	0.9572	0.6493	0.8628	0.039*
H13B	0.9464	0.5360	0.9186	0.039*
C14	1.1659 (5)	0.5563 (4)	0.8579 (2)	0.0303 (9)
H14A	1.1755	0.4755	0.8667	0.036*
H14B	1.1569	0.5712	0.7918	0.036*
C15	1.1471 (5)	0.7610 (3)	0.9650 (3)	0.0314 (8)
H15A	1.1927	0.7963	1.0206	0.038*
H15B	1.0701	0.8131	0.9361	0.038*
C16	1.2827 (5)	0.7362 (3)	0.8985 (2)	0.0279 (8)
H16A	1.2516	0.7618	0.8366	0.033*
H16B	1.3814	0.7755	0.9183	0.033*
C17	1.4589 (5)	0.5863 (4)	0.8441 (3)	0.0345 (9)
H17A	1.5547	0.6134	0.8782	0.041*
H17B	1.4522	0.6265	0.7855	0.041*
C18	1.4796 (5)	0.4631 (4)	0.8249 (3)	0.0348 (9)
H18A	1.4422	0.4199	0.8773	0.042*
H18B	1.4131	0.4424	0.7708	0.042*
C19	1.6527 (5)	0.4346 (4)	0.8082 (3)	0.0385 (10)
H19A	1.6602	0.3550	0.7935	0.046*
H19B	1.7167	0.4477	0.8648	0.046*
C20	1.7244 (6)	0.5012 (4)	0.7312 (3)	0.0417 (11)
H20A	1.6572	0.4932	0.6760	0.062*
H20B	1.8321	0.4739	0.7197	0.062*
H20C	1.7300	0.5793	0.7485	0.062*

Atomic displacement parameters (Å^2)

	U^{11}	U^{22}	U^{33}	U^{12}	U^{13}	U^{23}
Co1	0.0326 (3)	0.0238 (3)	0.0327 (2)	−0.0009 (2)	−0.0002 (2)	0.0029 (2)
Cl1	0.0502 (6)	0.0355 (6)	0.0288 (4)	−0.0037 (5)	0.0015 (4)	−0.0005 (4)
Cl2	0.0429 (6)	0.0268 (5)	0.0546 (6)	0.0019 (5)	−0.0071 (5)	0.0055 (4)

A21

Cl3	0.0385 (5)	0.0285 (5)	0.0454 (5)	−0.0021 (4)	0.0099 (4)	0.0031 (4)
N1	0.0319 (17)	0.0216 (17)	0.0260 (13)	0.0059 (13)	0.0046 (12)	0.0006 (12)
N2	0.0305 (18)	0.0259 (18)	0.0271 (15)	0.0015 (14)	0.0002 (13)	−0.0009 (12)
C1	0.034 (2)	0.023 (2)	0.0347 (18)	0.0029 (17)	0.0007 (15)	0.0025 (15)
C2	0.036 (2)	0.024 (2)	0.0297 (18)	0.0071 (16)	0.0058 (16)	−0.0001 (14)
C3	0.035 (2)	0.036 (2)	0.0273 (17)	0.0080 (18)	0.0036 (15)	−0.0027 (15)
C4	0.035 (2)	0.026 (2)	0.0349 (19)	0.0051 (17)	0.0052 (16)	−0.0050 (15)
C5	0.040 (2)	0.028 (2)	0.0277 (17)	−0.0031 (18)	0.0017 (15)	0.0001 (14)
C6	0.041 (2)	0.031 (2)	0.0230 (16)	−0.0036 (19)	0.0033 (15)	0.0048 (14)
C7	0.040 (2)	0.036 (2)	0.0294 (18)	0.0053 (19)	0.0000 (16)	−0.0029 (15)
C8	0.058 (3)	0.045 (3)	0.040 (2)	−0.015 (2)	−0.005 (2)	−0.0049 (19)
C9	0.045 (3)	0.077 (4)	0.040 (2)	−0.015 (3)	0.005 (2)	−0.018 (2)
C10	0.086 (5)	0.118 (7)	0.054 (3)	−0.066 (5)	0.020 (3)	−0.032 (4)
Co2	0.0293 (3)	0.0241 (3)	0.0285 (2)	−0.0002 (2)	0.00579 (18)	−0.0004 (2)
Cl4	0.0406 (6)	0.0265 (5)	0.0415 (5)	−0.0042 (4)	0.0101 (4)	0.0004 (4)
Cl5	0.0366 (5)	0.0301 (6)	0.0414 (5)	0.0042 (4)	−0.0033 (4)	−0.0018 (4)
Cl6	0.0415 (5)	0.0306 (5)	0.0276 (4)	−0.0026 (5)	0.0055 (4)	−0.0014 (4)
N3	0.0284 (17)	0.0228 (17)	0.0258 (14)	−0.0007 (13)	0.0045 (12)	−0.0004 (11)
N4	0.0296 (17)	0.0228 (17)	0.0276 (15)	−0.0018 (14)	0.0030 (12)	−0.0029 (12)
C11	0.033 (2)	0.041 (2)	0.0269 (17)	0.0037 (19)	0.0052 (15)	0.0063 (16)
C12	0.034 (2)	0.0229 (19)	0.0305 (17)	0.0007 (16)	0.0021 (15)	0.0017 (14)
C13	0.028 (2)	0.039 (2)	0.0296 (18)	−0.0032 (18)	0.0005 (15)	−0.0075 (16)
C14	0.028 (2)	0.032 (2)	0.0308 (18)	−0.0036 (17)	0.0071 (15)	−0.0063 (15)
C15	0.040 (2)	0.021 (2)	0.0335 (18)	−0.0005 (17)	0.0088 (17)	0.0034 (14)
C16	0.030 (2)	0.026 (2)	0.0269 (17)	−0.0035 (15)	0.0037 (15)	0.0036 (14)
C17	0.035 (2)	0.035 (2)	0.035 (2)	−0.0053 (19)	0.0128 (17)	−0.0069 (17)
C18	0.037 (2)	0.031 (2)	0.036 (2)	−0.0011 (18)	0.0072 (17)	−0.0030 (16)
C19	0.034 (2)	0.046 (3)	0.036 (2)	0.006 (2)	0.0090 (18)	0.0050 (19)
C20	0.045 (3)	0.046 (3)	0.035 (2)	−0.003 (2)	0.0141 (19)	−0.0008 (19)

Geometric parameters (Å, °)

Co1—N1	2.096 (3)	Co2—N3	2.088 (3)
Co1—Cl2	2.2483 (13)	Co2—Cl4	2.2482 (12)
Co1—Cl1	2.2491 (12)	Co2—Cl5	2.2487 (12)
Co1—Cl3	2.2521 (11)	Co2—Cl6	2.2564 (11)
N1—C1	1.486 (5)	N3—C15	1.477 (5)
N1—C3	1.491 (5)	N3—C13	1.493 (5)
N1—C5	1.491 (5)	N3—C11	1.495 (5)
N2—C7	1.500 (6)	N4—C14	1.507 (5)
N2—C2	1.505 (5)	N4—C16	1.508 (5)
N2—C6	1.520 (5)	N4—C12	1.516 (5)
N2—C4	1.536 (5)	N4—C17	1.524 (5)
C1—C2	1.537 (6)	C11—C12	1.536 (6)
C1—H1A	0.9900	C11—H11A	0.9900
C1—H1B	0.9900	C11—H11B	0.9900
C2—H2A	0.9900	C12—H12A	0.9900
C2—H2B	0.9900	C12—H12B	0.9900
C3—C4	1.530 (6)	C13—C14	1.530 (5)

C3—H3A	0.9900	C13—H13A	0.9900
C3—H3B	0.9900	C13—H13B	0.9900
C4—H4A	0.9900	C14—H14A	0.9900
C4—H4B	0.9900	C14—H14B	0.9900
C5—C6	1.517 (6)	C15—C16	1.550 (5)
C5—H5A	0.9900	C15—H15A	0.9900
C5—H5B	0.9900	C15—H15B	0.9900
C6—H6A	0.9900	C16—H16A	0.9900
C6—H6B	0.9900	C16—H16B	0.9900
C7—C8	1.510 (7)	C17—C18	1.530 (6)
C7—H7A	0.9900	C17—H17A	0.9900
C7—H7B	0.9900	C17—H17B	0.9900
C8—C9	1.522 (7)	C18—C19	1.518 (6)
C8—H8A	0.9900	C18—H18A	0.9900
C8—H8B	0.9900	C18—H18B	0.9900
C9—C10	1.508 (9)	C19—C20	1.528 (6)
C9—H9A	0.9900	C19—H19A	0.9900
C9—H9B	0.9900	C19—H19B	0.9900
C10—H10A	0.9800	C20—H20A	0.9800
C10—H10B	0.9800	C20—H20B	0.9800
C10—H10C	0.9800	C20—H20C	0.9800
N1—Co1—Cl2	106.21 (10)	N3—Co2—Cl4	107.62 (10)
N1—Co1—Cl1	102.29 (9)	N3—Co2—Cl5	104.35 (9)
Cl2—Co1—Cl1	113.39 (5)	Cl4—Co2—Cl5	111.41 (5)
N1—Co1—Cl3	103.81 (9)	N3—Co2—Cl6	101.11 (10)
Cl2—Co1—Cl3	114.25 (5)	Cl4—Co2—Cl6	116.46 (4)
Cl1—Co1—Cl3	115.14 (5)	Cl5—Co2—Cl6	114.35 (5)
C1—N1—C3	108.0 (3)	C15—N3—C13	108.1 (3)
C1—N1—C5	107.9 (3)	C15—N3—C11	108.1 (3)
C3—N1—C5	108.2 (3)	C13—N3—C11	108.7 (3)
C1—N1—Co1	112.5 (2)	C15—N3—Co2	112.2 (2)
C3—N1—Co1	109.8 (2)	C13—N3—Co2	110.7 (2)
C5—N1—Co1	110.3 (2)	C11—N3—Co2	108.9 (2)
C7—N2—C2	109.7 (3)	C14—N4—C16	109.0 (3)
C7—N2—C6	112.7 (3)	C14—N4—C12	109.5 (3)
C2—N2—C6	107.1 (3)	C16—N4—C12	107.1 (3)
C7—N2—C4	110.5 (3)	C14—N4—C17	110.9 (3)
C2—N2—C4	108.8 (3)	C16—N4—C17	110.2 (3)
C6—N2—C4	108.0 (3)	C12—N4—C17	110.1 (3)
N1—C1—C2	110.5 (3)	N3—C11—C12	110.6 (3)
N1—C1—H1A	109.5	N3—C11—H11A	109.5
C2—C1—H1A	109.5	C12—C11—H11A	109.5
N1—C1—H1B	109.5	N3—C11—H11B	109.5
C2—C1—H1B	109.5	C12—C11—H11B	109.5
H1A—C1—H1B	108.1	H11A—C11—H11B	108.1
N2—C2—C1	109.6 (3)	N4—C12—C11	108.4 (3)
N2—C2—H2A	109.8	N4—C12—H12A	110.0
C1—C2—H2A	109.8	C11—C12—H12A	110.0
N2—C2—H2B	109.8	N4—C12—H12B	110.0

A23

C1—C2—H2B	109.8	C11—C12—H12B	110.0
H2A—C2—H2B	108.2	H12A—C12—H12B	108.4
N1—C3—C4	110.4 (3)	N3—C13—C14	110.2 (3)
N1—C3—H3A	109.6	N3—C13—H13A	109.6
C4—C3—H3A	109.6	C14—C13—H13A	109.6
N1—C3—H3B	109.6	N3—C13—H13B	109.6
C4—C3—H3B	109.6	C14—C13—H13B	109.6
H3A—C3—H3B	108.1	H13A—C13—H13B	108.1
C3—C4—N2	109.0 (3)	N4—C14—C13	109.4 (3)
C3—C4—H4A	109.9	N4—C14—H14A	109.8
N2—C4—H4A	109.9	C13—C14—H14A	109.8
C3—C4—H4B	109.9	N4—C14—H14B	109.8
N2—C4—H4B	109.9	C13—C14—H14B	109.8
H4A—C4—H4B	108.3	H14A—C14—H14B	108.3
N1—C5—C6	112.0 (3)	N3—C15—C16	111.0 (3)
N1—C5—H5A	109.2	N3—C15—H15A	109.4
C6—C5—H5A	109.2	C16—C15—H15A	109.4
N1—C5—H5B	109.2	N3—C15—H15B	109.4
C6—C5—H5B	109.2	C16—C15—H15B	109.4
H5A—C5—H5B	107.9	H15A—C15—H15B	108.0
C5—C6—N2	108.3 (3)	N4—C16—C15	108.3 (3)
C5—C6—H6A	110.0	N4—C16—H16A	110.0
N2—C6—H6A	110.0	C15—C16—H16A	110.0
C5—C6—H6B	110.0	N4—C16—H16B	110.0
N2—C6—H6B	110.0	C15—C16—H16B	110.0
H6A—C6—H6B	108.4	H16A—C16—H16B	108.4
N2—C7—C8	114.7 (4)	N4—C17—C18	113.8 (3)
N2—C7—H7A	108.6	N4—C17—H17A	108.8
C8—C7—H7A	108.6	C18—C17—H17A	108.8
N2—C7—H7B	108.6	N4—C17—H17B	108.8
C8—C7—H7B	108.6	C18—C17—H17B	108.8
H7A—C7—H7B	107.6	H17A—C17—H17B	107.7
C7—C8—C9	112.8 (5)	C19—C18—C17	111.5 (4)
C7—C8—H8A	109.0	C19—C18—H18A	109.3
C9—C8—H8A	109.0	C17—C18—H18A	109.3
C7—C8—H8B	109.0	C19—C18—H18B	109.3
C9—C8—H8B	109.0	C17—C18—H18B	109.3
H8A—C8—H8B	107.8	H18A—C18—H18B	108.0
C10—C9—C8	111.6 (6)	C18—C19—C20	113.4 (4)
C10—C9—H9A	109.3	C18—C19—H19A	108.9
C8—C9—H9A	109.3	C20—C19—H19A	108.9
C10—C9—H9B	109.3	C18—C19—H19B	108.9
C8—C9—H9B	109.3	C20—C19—H19B	108.9
H9A—C9—H9B	108.0	H19A—C19—H19B	107.7
C9—C10—H10A	109.5	C19—C20—H20A	109.5
C9—C10—H10B	109.5	C19—C20—H20B	109.5
H10A—C10—H10B	109.5	H20A—C20—H20B	109.5
C9—C10—H10C	109.5	C19—C20—H20C	109.5
H10A—C10—H10C	109.5	H20A—C20—H20C	109.5

A24

H10B—C10—H10C	109.5	H20B—C20—H20C	109.5

Hydrogen-bond geometry (Å, °)

D—H···*A*	*D*—H	H···*A*	*D*···*A*	*D*—H···*A*
C2—H2B···Cl6^{i}	0.99	2.66	3.567 (5)	153
C4—H4A···Cl1^{ii}	0.99	2.66	3.511 (5)	145
C6—H6B···Cl3^{ii}	0.99	2.69	3.606 (5)	154
C7—H7B···Cl3^{iii}	0.99	2.80	3.729 (5)	157
C12—H12B···Cl5^{iv}	0.99	2.62	3.485 (4)	146
C14—H14A···Cl6^{iv}	0.99	2.75	3.567 (5)	140
C16—H16A···Cl1^{v}	0.99	2.60	3.548 (4)	161
C16—H16B···Cl5^{v}	0.99	2.81	3.739 (4)	156

Symmetry codes: (i) $x-1, y, z-1$; (ii) $-x, y-1/2, -z+1$; (iii) $x-1, y, z$; (iv) $-x+2, y-1/2, -z+2$; (v) $x+1, y, z$.

A25

Acta Crystallographica Section E
Structure Reports
Online

ISSN 1600-5368

Intercalated brucite-type layered cobalt(II) hydroxysulfate

Bunlawee Yotnoi,[a] Sanchai Luachan,[a] Timothy J. Prior[b] and Apinpus Rujiwatra[a]*

[a]Department of Chemistry, Faculty of Science, Chiang Mai University, Chiang Mai 50200, Thailand, and [b]Department of Chemistry, University of Hull, Kingston upon Hull HU6 7RX, England
Correspondence e-mail: apinpus@chiangmai.ac.th

Received 27 May 2009; accepted 12 June 2009

Key indicators: single-crystal X-ray study; T = 150 K; mean σ(S–O) = 0.006 Å; disorder in main residue; R factor = 0.048; wR factor = 0.132; data-to-parameter ratio = 12.4.

In an attempt to synthesize new cobalt(II) sulfate framework structures using 1,4-diazabicyclo[2.2.2]octane as a template, crystals of poly[0.35-[hexaaquacobalt(II)] [tri-μ-hydroxido-μ-sulfato-dicobalt(II)]], $\{[Co(H_2O)_6]_{0.35}[Co_2(OH)_3(SO_4)]\}_n$, were obtained as a mixture with $[Co(H_2O)_6]SO_4$ crystals. The crystal structure can be described as being constructed from discrete brucite-type $[Co_4(OH)_6(SO_4)_2]$ layers, each of which is built up from edge-shared $[Co(OH)_6]$ and $[Co(OH)_4(OSO_3)_2]$ octahedra, with partial intercalation by $[Co(H_2O)_6]^{2+}$ ions. The absence of *ca* 30% of the $[Co(H_2O)_6]^{2+}$ cations indicates partial oxidation of cobalt(II) to cobalt(III) within the layer.

Related literature

The crystal structure of the title compound is closely related to that of $Co_5(OH)_6(SO_4)_2(H_2O)_4$ (Ben Salah *et al.*, 2004, 2006), which is composed of brucite-type cobalt hydroxide layers. The fundamental difference lies in the way that adjacent layers are linked; being pillared by $\cdots O_3SO{-}Co(H_2O)_4{-}OSO_3\cdots$ groups in $Co_5(OH)_6(SO_4)_2(H_2O)_4$ but partially intercalated by $[Co(H_2O)_6]^{2+}$ ions in the title compound. For the crystal structures of layered materials of this type, see: Poudret *et al.* (2008). For a description of the Cambridge Structural Database, see: Allen (2002).

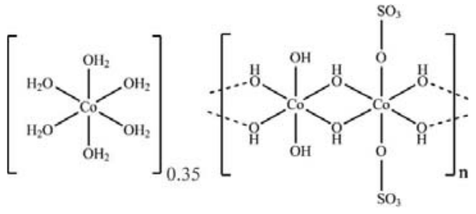

Experimental

Crystal data

$[Co(H_2O)_6]_{0.35}[Co_2(OH)_3(SO_4)]$
M_r = 323.41
Trigonal, $P\bar{3}m1$
a = 6.3627 (19) Å
c = 12.180 (4) Å
V = 427.0 (2) Å^3
Z = 2
Mo $K\alpha$ radiation
μ = 4.80 mm^{-1}
T = 150 K
0.21 × 0.13 × 0.03 mm

Data collection

Stoe IPDS2 diffractometer
Absorption correction: multi-scan (*X-RED*; Stoe & Cie, 2008)
T_{min} = 0.415, T_{max} = 0.862
1663 measured reflections
497 independent reflections
325 reflections with $I > 2\sigma(I)$
R_{int} = 0.097

Refinement

$R[F^2 > 2\sigma(F^2)]$ = 0.048
$wR(F^2)$ = 0.132
S = 0.90
497 reflections
40 parameters
3 restraints
Only H-atom coordinates refined
$\Delta\rho_{max}$ = 1.04 e Å^{-3}
$\Delta\rho_{min}$ = −1.05 e Å^{-3}

Data collection: *X-AREA* (Stoe & Cie, 2008); cell refinement: *X-AREA*; data reduction: *X-RED* (Stoe & Cie, 2008); program(s) used to solve structure: *SHELXS86* (Sheldrick, 2008); program(s) used to refine structure: *SHELXL97* (Sheldrick, 2008); molecular graphics: *DIAMOND* (Brandenburg & Putz, 1999); software used to prepare material for publication: *PLATON* (Spek, 2009).

The authors thank the Thailand Research Fund, the Center for Innovation in Chemistry and the Thailand Toray Science Foundation for financial support. BY thanks the Royal Golden Jubilee PhD program and the Graduate School of Chiang Mai University for a Graduate Scholarship.

Supplementary data and figures for this paper are available from the IUCr electronic archives (Reference: LH2832).

References

Allen, F. H. (2002). *Acta Cryst.* B**58**, 380–388.
Ben Salah, M., Vilminot, S., Andre, G., Richard-Plouet, M., Mhiri, T., Takagi, S. & Kurmoo, M. (2006). *J. Am. Chem. Soc.* **128**, 7972–7981.
Ben Salah, M., Vilminot, S., Richard-Plouet, M., Andre, G., Mhiri, T. & Kurmoo, M. (2004). *Chem. Commun.* pp. 2548–2549.
Brandenburg, K. & Putz, H. (1999). *DIAMOND*. Crystal Impact GbR, Bonn, Germany.
Poudret, L., Prior, T. J., McIntyre, L. J. & Fogg, A. M. (2008). *Chem. Mater.* **20**, 7447–7453.
Sheldrick, G. M. (2008). *Acta Cryst.* A**64**, 112–122.
Spek, A. L. (2009). *Acta Cryst.* D**65**, 148–155.
Stoe & Cie (2008). *X-AREA* and *X-RED*. Stoe & Cie, Darmstadt, Germany.

i52 Yotnoi *et al.* doi:10.1107/S160053680902251X *Acta Cryst.* (2009). E**65**, i52

A26

Acta Cryst. (2009). E**65**, i52 [**doi:10.1107/S160053680902251X**]

Intercalated brucite-type layered cobalt(II) hydroxysulfate

B. Yotnoi, S. Luachan, T. J. Prior and A. Rujiwatra

Comment

Layered transition-metal hydroxides, in particular those exhibiting the brucite structure, have gained serious interest in both chemical and physical aspects. While the intercalation chemistry and potential application as catalysts are of the prime interest for the chemists, the physical interest primarily stems from the long-rang magnetic ordering in two dimensions. Examples of two dimensional triangular networks exhibiting such ordering are very rare, and the information on the crystal structures of layered materials of this type is yet rarer (Poudret, 2008). Thusfar there has been only one structure, $Co_5(OH)_6(SO_4)_2(H_2O)_4$, having the truely brucite-type magnetic layer (Ben Salah et al., 2004). The nuclear and magnetic structures, and magnetic properties of the compound were extensively reported (Ben Salah et al., 2006). The crystal structure of $Co_5(OH)_6(SO_4)_2(H_2O)_4$ consists of brucite-type cobalt hydroxide layers of edge-sharing octahedra, which are pillared by $\cdots O_3SO—Co(H_2O)_4—OSO_3\cdots$ groups. The compound exhibits ferromagnetic coupling with purely two dimensional magnetic ordering in an easy-plane magnet, which is a rare example of a single-layer magnet.

The crystal structure of $[Co(H_2O)_6]_x[Co_4(SO_4)_2(OH)_6]$ (I) where x ≃ 0.70 is closely related to that of $Co_5(OH)_6(SO_4)_2(H_2O)_4$ (Fig. 1), also comprised of brucite-type $[Co_4(SO_4)_2(OH)_6]$ layers, each of which is built up from the edge-shared $[Co(OH)_6]$ and $[Co(OH)_4(OSO_3)_2]$ octahedra in the ab plane (Fig. 2). Two of three crystallographically distinct cobalt ions (Fig. 3), Co1 and Co2, are within the layers and located on the 1b and 3f Wyckoff sites, respectively. Unlike the $Co_5(OH)_6(SO_4)_2(H_2O)_4$ structure, the sulfate anion acts as a monodentate ligand and is coordinate covalently connected to the layered Co2 ion via the apical O atom, leaving the three basal O atoms pointing into the interlayered space (Fig. 3). The $[Co_4(SO_4)_2(OH)_6]$ layers are stacked in the ABAB fashion along c, with a repeat distance of 12.180 (4) Å. In the interlayered gallery, there are intercalated discrete $[Co(H_2O)_6]^{2+}$ ions in which the Co3 is located on the 1a site. These $[Co(H_2O)_6]^{2+}$ ions are aligned in a way to maximize the hydrogen bonding interactions of O—H···O type between the aquo ligands and the basal O atoms of the layered sulfate pendants (Fig. 1). The orientation of the sulfate is also regulated by the hydrogen bonds established between the sulfate basal O atoms and the layered hydroxy groups. The Co—O bond length (2.065 (8) Å) within the hexaaquo ion is in good agreement with similar cations in the Cambridge Structural Database (Allen, 2002). The mean of similar Co—O distances is 2.09 (3) Å, but is notable that the majority of these structures were collected at room temperature. 97% of the structures containing cobalt hexaaquo ions are explicitly recorded at Co^{2+}, none are recorded as Co^{3+}.

The refined site occupancy of the intercalated $[Co(H_2O)_6]^{2+}$ ions and the assumption of total charge neutrality imply the partial oxidation (15%) of the layer Co^{II} to Co^{III}. This yields an overall composition $[Co^{II}(H_2O)_6]_{0.7}[Co^{II}_{3.4}Co^{III}_{0.6}(SO_4)_2(OH)_6]$ for I .

A27

Experimental

In the attempt to synthesize new cobalt(II) sulfate frameworks, crystals of **I** were unintentionally obtained from the hydrothermal reaction of cobalt(II) sulfate heptahydrate and 1,4-diazabicyclo[2.2.2]octane in acidic aqueous solution (pH 4.4) under autogenous pressure at 453 K for 72 h.

Refinement

Hydrogen atoms were located by difference Fourier methods. The positions of these were refined subject to weak bond length restraints. Displacement parameters for the hydrogen atoms were set at 1.5 times the isotropic diaplcement parameter of the oxygen atom.

Prior to the refinement of site ocupancy of $[Co(H_2O)_6]^{2+}$, all atoms were located using Fourier difference methods. The displacement parameters of the intercalating ion were anomalously large. There were large maxima and minima in the residual electron density: e-max = 2.59 e Å^{-3} (centered on Co2); e-min = -2.58 e Å^{-3}. At this stage $wR(F^2) = 0.1914$.

Refinement of the occupancy of the $[Co(H_2O)_6]^{2+}$ cation resulted in a significant improvement in the quality of the fit to the data: e-max = 1.044 e Å^{-3}; e-min = -1.046 e Å^{-3} and $wR(F^2) = 0.132$.

Careful inspection of the diffraction images did not reveal any weak reflections which might indicate ordering of the partially occupied cation.

Figures

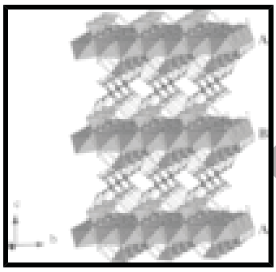

Fig. 1. View of the crystal structure of **I** along the *a* axis showing the brucite-type $[Co_4(SO_4)_2(OH)_6]$ layers which are intercalatated by the hydrogen bonded (dash lines) $[Co(H_2O)_6]^{2+}$ ions.

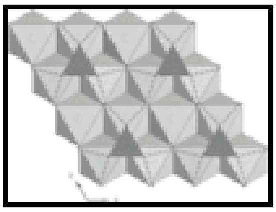

Fig. 2. Polyhedral representation of the cobalt hydroxysulate layer, built up of the edge-shared $[Co(OH)_6]$ and $[Co(OH)_4(OSO_3)_2]$ octahedra.

A28

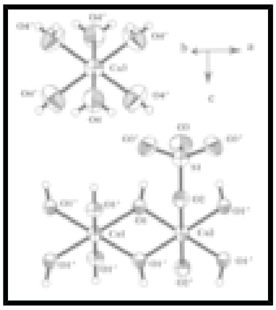

Fig. 3. View of the extended asymmetric unit of **I** with atom numbering scheme. Displacement ellipsoids are drawn at the 80% probability level.

poly[0.35-[hexaaquacobalt(II)] [tri-μ-hydroxido-μ-sulfato-dicobalt(II)]]

Crystal data

$[Co(H_2O)_6]_{0.35}[Co_2(OH)_3(SO_4)]$

$M_r = 323.41$

Trigonal, $P\bar{3}m1$

Hall symbol: -P 3 2"

$a = 6.3627$ (19) Å

$b = 6.3627$ (19) Å

$c = 12.180$ (4) Å

$\alpha = 90°$

$\beta = 90°$

$\gamma = 120°$

$V = 427.0$ (2) Å^3

$Z = 2$

$F_{000} = 318.9$

$D_x = 2.515$ Mg m^{-3}

Mo $K\alpha$ radiation, $\lambda = 0.71073$ Å

Cell parameters from 1764 reflections

$\theta = 1.7–29.3°$

$\mu = 4.80$ mm^{-1}

$T = 150$ K

Plate, pale pink

0.21 × 0.13 × 0.03 mm

Data collection

Stoe IPDS2
diffractometer

Radiation source: fine-focus sealed tube

Monochromator: graphite

Detector resolution: 6.67 pixels mm^{-1}

$T = 150$ K

ω scans

Absorption correction: multi-scan
(X-RED; Stoe & Cie, 2008)

$T_{min} = 0.415$, $T_{max} = 0.862$

1663 measured reflections

497 independent reflections

325 reflections with $I > 2\sigma(I)$

$R_{int} = 0.097$

$\theta_{max} = 29.3°$

$\theta_{min} = 1.7°$

$h = -7 \rightarrow 8$

$k = -7 \rightarrow 8$

$l = -14 \rightarrow 16$

Refinement

Refinement on F^2

Least-squares matrix: full

$R[F^2 > 2\sigma(F^2)] = 0.048$

$wR(F^2) = 0.132$

Secondary atom site location: difference Fourier map

Hydrogen site location: difference Fourier map

Only H-atom coordinates refined

$w = 1/[\sigma^2(F_o^2) + (0.0839P)^2]$
where $P = (F_o^2 + 2F_c^2)/3$

A29

$S = 0.90$

497 reflections

40 parameters

3 restraints

Primary atom site location: structure-invariant direct methods

$(\Delta/\sigma)_{max} < 0.001$

$\Delta\rho_{max} = 1.04$ e Å^{-3}

$\Delta\rho_{min} = -1.05$ e Å^{-3}

Extinction correction: none

Special details

Geometry. All e.s.d.'s (except the e.s.d. in the dihedral angle between two l.s. planes) are estimated using the full covariance matrix. The cell e.s.d.'s are taken into account individually in the estimation of e.s.d.'s in distances, angles and torsion angles; correlations between e.s.d.'s in cell parameters are only used when they are defined by crystal symmetry. An approximate (isotropic) treatment of cell e.s.d.'s is used for estimating e.s.d.'s involving l.s. planes.

Refinement. Refinement of F^2 against ALL reflections. The weighted R-factor wR and goodness of fit S are based on F^2, conventional R-factors R are based on F, with F set to zero for negative F^2. The threshold expression of $F^2 > \sigma(F^2)$ is used only for calculating R-factors(gt) *etc*. and is not relevant to the choice of reflections for refinement. R-factors based on F^2 are statistically about twice as large as those based on F, and R- factors based on ALL data will be even larger.

Fractional atomic coordinates and isotropic or equivalent isotropic displacement parameters (Å^2)

	x	y	z	U_{iso}*/U_{eq}	Occ. (<1)
Co2	0.5000	0.0000	0.5000	0.0170 (3)	
Co1	0.0000	0.0000	0.5000	0.0163 (5)	
S1	0.6667	0.3333	0.2679 (2)	0.0214 (6)	
O1	0.1717 (3)	−0.1717 (3)	0.4215 (3)	0.0164 (9)	
O2	0.6667	0.3333	0.3913 (6)	0.0188 (15)	
O3	0.5403 (5)	0.0807 (9)	0.2298 (4)	0.0292 (11)	
Co3	0.0000	0.0000	0.0000	0.0250 (11)	0.700 (11)
O4	0.1574 (8)	0.3148 (16)	0.0920 (7)	0.039 (2)	0.700 (11)
H1	0.188 (9)	−0.188 (9)	0.355 (3)	0.059*	
H4	0.073 (9)	0.353 (18)	0.128 (5)	0.059*	0.700 (11)

Atomic displacement parameters (Å^2)

	U^{11}	U^{22}	U^{33}	U^{12}	U^{13}	U^{23}
Co2	0.0146 (5)	0.0156 (6)	0.0211 (6)	0.0078 (3)	0.0001 (2)	0.0002 (4)
Co1	0.0144 (6)	0.0144 (6)	0.0202 (9)	0.0072 (3)	0.000	0.000
S1	0.0220 (9)	0.0220 (9)	0.0203 (12)	0.0110 (4)	0.000	0.000
O1	0.0177 (16)	0.0177 (16)	0.0167 (18)	0.0111 (17)	−0.0002 (8)	0.0002 (8)
O2	0.017 (2)	0.017 (2)	0.023 (4)	0.0083 (11)	0.000	0.000
O3	0.034 (2)	0.023 (2)	0.027 (2)	0.0116 (12)	−0.0034 (10)	−0.0069 (19)
Co3	0.0256 (13)	0.0256 (13)	0.0238 (17)	0.0128 (7)	0.000	0.000
O4	0.034 (3)	0.043 (5)	0.044 (4)	0.022 (2)	−0.0080 (18)	−0.016 (4)

Geometric parameters (Å, °)

Co2—O1	2.047 (3)	S1—O3^{ix}	1.467 (5)

A30

Co2—O1^{i}	2.047 (3)	S1—O2	1.502 (7)
Co2—O1^{ii}	2.047 (3)	O1—Co2^{x}	2.047 (3)
Co2—O1^{iii}	2.047 (3)	O1—H1	0.83 (3)
Co2—O2	2.264 (4)	O2—Co2^{viii}	2.264 (4)
Co2—O2^{i}	2.264 (4)	O2—Co2^{ix}	2.264 (4)
Co1—O1^{iv}	2.121 (4)	Co3—O4^{xi}	2.065 (8)
Co1—O1^{iii}	2.121 (4)	Co3—O4	2.065 (8)
Co1—O1^{v}	2.121 (4)	Co3—O4^{iv}	2.065 (8)
Co1—O1^{vi}	2.121 (4)	Co3—O4^{vi}	2.065 (8)
Co1—O1	2.121 (4)	Co3—O4^{xii}	2.065 (8)
Co1—O1^{vii}	2.121 (4)	Co3—O4^{xiii}	2.065 (8)
S1—O3	1.467 (5)	O4—H4	0.82 (3)
S1—O3^{viii}	1.467 (5)		

O1—Co2—O1^{i}	180.000 (1)	O3^{viii}—S1—O3^{ix}	110.49 (19)
O1—Co2—O1^{ii}	97.8 (2)	O3—S1—O2	108.4 (2)
O1^{i}—Co2—O1^{ii}	82.2 (2)	O3^{viii}—S1—O2	108.4 (2)
O1—Co2—O1^{iii}	82.2 (2)	O3^{ix}—S1—O2	108.4 (2)
O1^{i}—Co2—O1^{iii}	97.8 (2)	Co2—O1—Co2^{x}	102.00 (17)
O1^{ii}—Co2—O1^{iii}	180.0 (2)	Co2—O1—Co1	99.51 (14)
O1—Co2—O2	95.83 (13)	Co2^{x}—O1—Co1	99.51 (14)
O1^{i}—Co2—O2	84.17 (13)	Co2—O1—H1	112 (4)
O1^{ii}—Co2—O2	95.83 (13)	Co2^{x}—O1—H1	112 (4)
O1^{iii}—Co2—O2	84.17 (13)	Co1—O1—H1	129 (7)
O1—Co2—O2^{i}	84.17 (13)	S1—O2—Co2^{viii}	125.79 (14)
O1^{i}—Co2—O2^{i}	95.83 (13)	S1—O2—Co2	125.79 (14)
O1^{ii}—Co2—O2^{i}	84.17 (13)	Co2^{viii}—O2—Co2	89.3 (2)
O1^{iii}—Co2—O2^{i}	95.83 (13)	S1—O2—Co2^{ix}	125.79 (14)
O2—Co2—O2^{i}	180.0	Co2^{viii}—O2—Co2^{ix}	89.3 (2)
O1^{iv}—Co1—O1^{iii}	180.0 (2)	Co2—O2—Co2^{ix}	89.3 (2)
O1^{iv}—Co1—O1^{v}	78.77 (13)	O4^{xi}—Co3—O4	180.0 (4)
O1^{iii}—Co1—O1^{v}	101.23 (13)	O4^{xi}—Co3—O4^{iv}	86.7 (4)
O1^{iv}—Co1—O1^{vi}	101.23 (13)	O4—Co3—O4^{iv}	93.3 (4)
O1^{iii}—Co1—O1^{vi}	78.77 (13)	O4^{xi}—Co3—O4^{vi}	86.7 (4)
O1^{v}—Co1—O1^{vi}	180.00 (15)	O4—Co3—O4^{vi}	93.3 (4)
O1^{iv}—Co1—O1	101.23 (13)	O4^{iv}—Co3—O4^{vi}	93.3 (4)
O1^{iii}—Co1—O1	78.77 (13)	O4^{xi}—Co3—O4^{xii}	93.3 (4)
O1^{v}—Co1—O1	78.77 (13)	O4—Co3—O4^{xii}	86.7 (4)
O1^{vi}—Co1—O1	101.23 (13)	O4^{iv}—Co3—O4^{xii}	86.7 (4)
O1^{iv}—Co1—O1^{vii}	78.77 (13)	O4^{vi}—Co3—O4^{xii}	180.0 (4)
O1^{iii}—Co1—O1^{vii}	101.23 (13)	O4^{xi}—Co3—O4^{xiii}	93.3 (4)
O1^{v}—Co1—O1^{vii}	101.23 (13)	O4—Co3—O4^{xiii}	86.7 (4)

O1$^{\mathrm{vi}}$—Co1—O1$^{\mathrm{vii}}$	78.77 (13)	O4$^{\mathrm{iv}}$—Co3—O4$^{\mathrm{xiii}}$	180.0 (4)
O1—Co1—O1$^{\mathrm{vii}}$	180.0 (2)	O4$^{\mathrm{vi}}$—Co3—O4$^{\mathrm{xiii}}$	86.7 (4)
O3—S1—O3$^{\mathrm{viii}}$	110.49 (19)	O4$^{\mathrm{xii}}$—Co3—O4$^{\mathrm{xiii}}$	93.3 (4)
O3—S1—O3$^{\mathrm{ix}}$	110.49 (19)	Co3—O4—H4	120 (5)

Symmetry codes: (i) $-x+1, -y, -z+1$; (ii) $-x+y+1, -x, z$; (iii) $x-y, x, -z+1$; (iv) $-x+y, -x, z$; (v) $y, -x+y, -z+1$; (vi) $-y, x-y, z$; (vii) $-x, -y, -z+1$; (viii) $-y+1, x-y, z$; (ix) $-x+y+1, -x+1, z$; (x) $-y, x-y-1, z$; (xi) $-x, -y, -z$; (xii) $y, -x+y, -z$; (xiii) $x-y, x, -z$.

Hydrogen-bond geometry (Å, °)

D—H···*A*	*D*—H	H···*A*	*D*···*A*	*D*—H···*A*
O1—H1···O3$^{\mathrm{x}}$	0.83 (3)	2.54 (5)	3.125 (6)	129 (4)
O1—H1···O3	0.83 (3)	2.54 (5)	3.125 (6)	129 (4)
O4—H4···O3$^{\mathrm{vi}}$	0.82 (3)	1.90 (9)	2.712 (1)	170 (7)

Symmetry codes: (x) $-y, x-y-1, z$; (vi) $-y, x-y, z$.

A32

Journal of Alloys and Compounds 475 (2009) 473–478

Contents lists available at ScienceDirect

Journal of Alloys and Compounds

journal homepage: www.elsevier.com/locate/jallcom

Fabrication and dielectric properties of lead titanate nanocomposites

R. Wongmaneerung[a], A. Rujiwatra[b], R. Yimnirun[c], S. Ananta[c,*]

[a] Department of Physics, Faculty of Science, Maejo University, Chiang Mai 50290, Thailand
[b] Department of Chemistry, Faculty of Science, Chiang Mai University, Chiang Mai 50200, Thailand
[c] Department of Physics, Faculty of Science, Chiang Mai University, Chiang Mai 50200, Thailand

ARTICLE INFO

Article history:
Received 14 January 2008
Received in revised form 8 July 2008
Accepted 13 July 2008
Available online 6 September 2008

Keywords:
Lead titanate
Perovskite
Composites
Microstructure
Dielectric properties

ABSTRACT

A simple powder mixing and pressure-less sintering process for fabrication of $PbTiO_3$ (PT) nanocomposites (micron-sized PT matrix reinforced with either PT nanoparticles or nanofibers) has been developed to enhance both densification and dielectric properties. The potentiality of a ceramic-nanocomposite technique as a low-cost and simple ceramic fabrication to obtain highly dense and pure PT/PT composites was demonstrated. It has been found that both densification and dielectric properties of the composites fabricated in this work were significantly enhanced, as compared to the two-stage sintering and the conventional PT ceramics.

1. Introduction

Pure and dense lead titanate ($PbTiO_3$ or PT) ceramic, which is of interest as a component in commercial electroceramic materials, is regarded to be one of the most difficult lead-based perovskite ferroelectric ceramics to produce [1–3]. The most important properties of PT ceramics are high Curie temperature (∼490 °C), large mechanical-quality factor and pyroelectric coefficient [4,5]. Moreover, PT when combined with other oxides can form a series of ferroelectric materials that exhibit many of the most desirable dielectric, piezoelectric and pyroelectric properties for use in electronic and electro-optic devices at high frequency and high temperature, such as infrared sensors, actuators and hydrophones [1–3]. However, PT ceramic is mechanically weak due to large distortion of the tetragonal phase at room temperature which is characterized by the ratio between the lattice parameters (c/a, hereafter called tetragonality, ∼1.06 [6,7]). Apart from general problems of PbO volatilization and associated high porosity, the stress induced by cooling through the phase transition can create cracking in bulk ceramics.

To overcome these problems, several techniques have been introduced, such as utilizing nanopowders, using additives, employing spark-plasma sintering and carrying out appropriated milling and sintering conditions [8–13]. All these techniques are aimed at reducing the lattice tetragonality of bulk ceramics, even though they inevitably affect the phase formation, structure and electrical properties of materials in different ways. Amongst all the issues reported so far, most attention has been concentrated on the use of additives and chemically derived powder processing, whereas investigations on modified particle packing or composite techniques have not been widely carried out [14,15].

Recently, ceramic-nanocomposites in which nanosized phases were dispersed within the matrix grains and/or at the grain boundaries have emerged as a novel approach of improving materials properties [16]. The mechanical properties of ceramics are known to be improved significantly by dispersing ceramic-nanoparticles into the ceramic-matrix grains or grain boundaries. However, the degree of improvement in their properties is dependent on the type of composite system involved [16]. Few studies have reported on ferroelectric matrix/metal nanodispersoid [17] and ferroelectric matrix/non-ferroelectric nanodispersoid [18] composite systems, and it is not yet clear how these dispersoids affect the properties of nanocomposites. Moreover, the problem of property trade-off, i.e., a deterioration of electrical properties still remains unsolved. In other words, the improvement of mechanical property can only be realized only by sacrificing electrical properties. So far, a little has been reported on the fabrication of ferroelectric matrix/ferroelectric nanodispersoid composite systems [19]. However, no work on the perovskite PT ceramic-nanocomposites has been reported yet.

Therefore, in this work, ferroelectric matrix/ferroelectric nanodispersoid PT composite has been developed to resolve these problems. With this new scheme, instead of using only micron-

---

[*] Corresponding author. Tel.: +66 53 943367; fax: +66 53 943445.
E-mail address: suponananta@yahoo.com (S. Ananta).

0925-8388/$ – see front matter © 2008 Elsevier B.V. All rights reserved.
doi:10.1016/j.jallcom.2008.07.074

A33

sized PT powders as reported in our previous works [13,20], two different types of PT nanodispersoid (nanoparticles and nanofibers) were adopted as starting materials. The influence of both PT nanodispersoids on densification, microstructure and dielectric properties of the composites will be discussed and compared with the conventional method.

2. Experimental procedure

The starting PT materials for the fabrication of self-reinforced PT matrix/PT nanodispersoid composites were micron-sized PT powders, nanopowders, and nanofibers (Fig. 1), which were synthesized via ball-milling, vibro-milling, and hydrothermal techniques, respectively. The characteristics of each starting PT materials and their processing details are described in our previous works [21–23]. The powder mixtures (matrix:dispersoid ratio of 1:1) were formed into pellets by adding 3 wt.% polyvinyl alcohol (PVA) binder, prior to pressing in a pseudo-uniaxial die press at 100 MPa. It should be noted here that preliminary study of other matrix:dispersoid ratios, e.g. 0.7:0.3 and 0.6:0.4 was carried out and the complete solid-solution microstructure type commonly observed in the conventional PT processing was observed in all cases, indicating the solubility effect of the perovskite PT/PT (although their morphologies are different) limiting the possibility of composite formation. Each pellet was placed in an alumina crucible together with an atmosphere powder of identical chemical composition [20]. Such a composite cannot be fabricated by hot-pressing in the reduced atmosphere because the Pb-based perovskite is easily decomposed in the atmosphere. In this work, the composites were prepared by using simple pressure-less sintering method. Sintering was carried out at various temperatures (1000–1225 °C), for 1 h with heating/cooling rates of 1 °C/min [13,20] applied. These firing conditions were advocated from our previous work on PT ceramics with experimental details presented in Refs. [13,20].

Densities of the sintered products were determined by using the Archimedes principle. X-ray diffraction (XRD; Siemens-D500 diffractometer) was carried out at room temperature using Cu Kα radiation to identify the phase formed. The lattice parameters and tetragonality factor (c/a) of the sintered ceramics were calculated from the XRD patterns [24]. The microstructural development was characterized using a scanning electron microscopy (SEM; JEOL JSM-840A), equipped with an energy dispersive X-ray (EDX) analyzer. Mean grain sizes of the sintered ceramics were subsequently estimated by employing the linear intercept method [25]. In order to evaluate the dielectric properties, densified ceramics were polished to form flat and parallel faces. The samples were coated with silver-paste electrodes which were fired on both sides of the samples at 700 °C for 1 h. The dielectric properties were measured using a HIOKI 3532-50 LCR meter, on cooling through the transition range (550–25 °C) with a rate of 5 °C/min at high frequencies ranging from 1 to 5 MHz. Values of the dielectric constant were corrected for porosity by using the relationship $\varepsilon_r = \varepsilon_{r(\text{measured})} \times$ theoretical density/sintered density [26].

3. Results and discussion

X-ray diffraction patterns of the PT composites reinforced with various PT dispersoids and sintered at various temperatures are displayed in Fig. 2, indicating the formation of single phase perovskite in all cases. The strongest reflections in the majority of all XRD traces indicate the formation of the PT perovskite phase of lead titanate which could be matched with JCPDS file no. 6-452, in agreement with other works [10–13]. To a first approximation, this phase has a tetragonal perovskite-type structure in space group $P4/mmm$ with cell parameters $a = 389.93$ pm and $c = 415.32$ pm [27]. All the peaks were assigned to PT, and no reaction phase between different PT starting materials was detected. Moreover, there is no significant difference between the PT nanocomposites reinforced with either PT nanopowders or nanofibers, after sintered at temperatures ranging from 1150 to 1200 °C. This observation could be attributed mainly to the high purity of the employed starting materials together with the optimized firing conditions. The samples sintered with temperature below 1150 °C were broken into pieces after sintering process, whilst the samples sintered at 1225 °C exhibited severe melted areas. Thus, no further characterization can be performed on these samples.

It should be noted that a single phase of perovskite is found in all PT composites similar with the two-stage sintering samples [20], in contrast to the observations for the conventional case [13] (Table 1). No evidence of pyrochlore phase of $PbTi_3O_7$ composition reported earlier by other workers [21,28] was found, nor was any evidence of other second phases [29] being present. This could be due to the lower firing temperature of the nanocomposite samples as compared to the conventional PT ceramics, leading to a smaller degree of lead losses and consequently avoiding the pyrochlore formation, in consistent with other works [30,31], whilst a sufficient arrangement of grain-packing required for ceramic densification still be reached. However, many other factors come into play, e.g. homogeneity of materials, reactivity of starting powders, and pro-

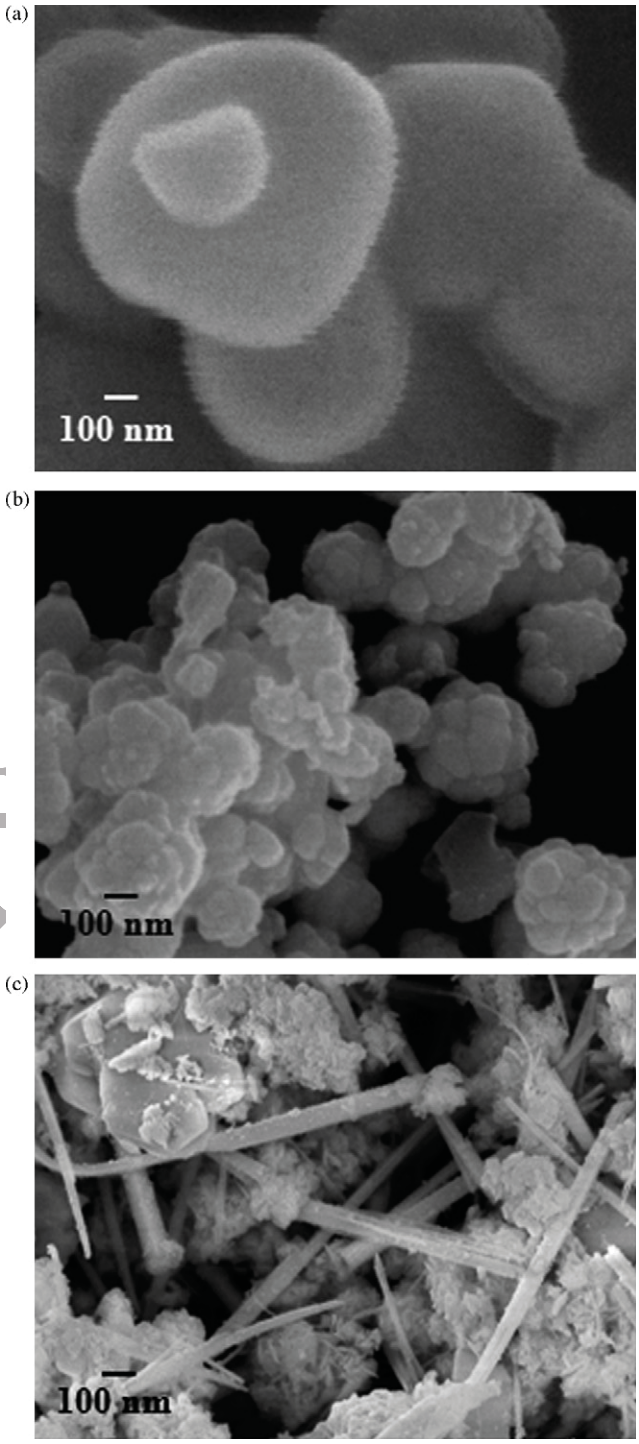

Fig. 1. SEM micrographs of the starting PT dispersoids: (a) micron-sized powders, (b) nanopowders, and (c) nanofibers.

A34

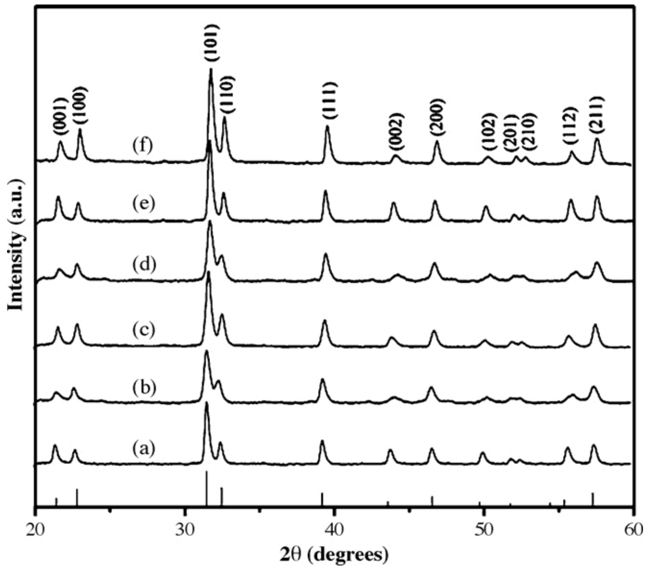

Fig. 2. XRD patterns of PT composites reinforced with PT nanopowders after sintered at (a) 1150 °C, (b) 1175 °C and (c) 1200 °C, and reinforced with PT nanofibers after sintered at (d) 1150 °C, (e) 1175 °C and (f) 1200 °C, for 2 h.

cessing variables. These XRD results clearly show that, in general, the different processing methods used for preparing PT ceramics gave rise to a different phase formation in the sintered materials. The absence of minor phase in composite samples was related to the more reactive process used.

Table 1 also shows tetragonality factor (c/a), relative density and average grain size of each nanocomposite sample, comparing with the conventional and the two-stage sintered samples, respectively. Generally, it is evident that as the sintering temperature increases, the density of almost all the samples increases. However, it can be seen that the sintering behavior of PT ceramics derived from different processing techniques were dissimilar. Two-stage sintering PT ceramics reached a maximum density of ~97% at 900/1200 °C [20]. Whilst conventional PT samples exhibit reduced densification, and a temperature of 1225 °C was required to reach a densification level of ~94% [13]. On the other hand, both types of PT nanocomposites sintered at 1200 °C exhibit the highest relative density of about 98% with a smallest average grain size of less than 1.0 μm. By comparison with conventional PT ceramics, lower values of tetragonality (c/a) are found in all nanocomposite cases, equivalent to those observed in the two-stage sintering case, indicating lower internal stress in these nanocomposites. More interestingly, all nanocomposite samples do not suffer from severe stresses as a result of the high c/a ratio so they have not broken into pieces after experienced the sintering process or once subjected to a cycle of high temperature measurement of dielectric properties, as reported previously for the conventional and two-stage sintering PT cases [13,20].

Microstructural features (free and fracture surfaces) of both PT nanocomposites sintered at different temperatures for 2 h are shown in Figs. 3 and 4. It was found that average grain sizes increase with the sintering temperature (Fig. 3). The PT nanodispersoids were found to locate both within the matrix and at the grain boundaries (see enlarged insertion in Fig. 3(d)). The microstructure of the composites is that of the nanocomposites classified as “nanomicro” and “nanofiber” types [16].

Representative fracture surfaces for both types of PT nanocomposites are given in Fig. 4. It is seen that a uniform grain shape of typical perovskite ceramics [9,30,31] is observed, with sizes in the range of 0.2–2.8 μm. It should be noted that the average grain size of both PT nanocomposites is <1.7 μm, which is less than the critical value of 3 μm [11,32,33] and gives rise to a volumetric percentage enough to buffer the anisotropic stress caused by the phase transition [32]. Here, it is believed that PT nanodispersoids with random orientations result in lower internal stress in composite samples because they compensate the anisotropy of thermal expansion coefficients.

By comparison with conventional PT ceramics [13], almost clean microstructures with highly uniform, denser angular grain-packing and more homogeneous are generally observed in both types of self-reinforced PT nanocomposites. These microstructures are typical of a solid-state sintering mechanism. In the present study (Figs. 3 and 4), the microstructural features of both types of PT nanocomposites with various sintering temperatures ranging from 1150 to 1200 °C are not significantly different. However, it should be noted that higher angularly grains were evidenced for higher sintering temperature. The observation that the sintering temperature effect may also play an important role in obtaining a high angularity grains of perovskite ceramics is also consistent with other similar systems [30,31]. Moreover, abnormal grain growth probably due to the inhibition of grain growth mechanism during doubly sintering process [20,34] was also found in some samples, as shown in Figs. 3(c and d) and 4(f). It is also of interest to point out that evidence of intergranular fracture has been found for the existence of microcracks (arrowed) along the grain boundaries of the composite samples self-reinforced with PT nanoparticles (Fig. 4(a–c)). The different microstructure evolution of PT nanocomposites confirms the importance of the processing method including the morphological characteristics of the dispersed phase, consistent with other works [32,35]. Whilst the grain size of both nanocomposites is approximately the same, the density and microstructure of PT samples sintered at higher temperatures indicated that the composite

Table 1

Sintering behavior of PT ceramics derived from different fabrication techniques

Processing [Ref.]	Sintering temperature (°C)	Perovskite phase[a] (%)	Relative density[b] (%)	Tetragonality factor (c/a)	Grain size[c] (μm)	Average grain size (μm)
Normal sintering [13]	1225	89.20	93.00	1.063	41.0–83.0	62.0
Two-stage sintering [20]	900/1200	100.00	97.02	1.061	1.0–2.2	1.6
Composite reinforced with nanopowders	1150	100.00	96.33	1.059	0.2–0.6	0.40
	1175	100.00	97.02	1.053	0.3–1.0	0.65
	1200	100.00	97.85	1.061	0.6–2.0	1.30
Composite reinforced with nanofibers	1150	100.00	95.68	1.053	0.3–1.3	0.80
	1175	100.00	96.76	1.058	0.4–1.3	0.85
	1200	100.00	97.45	1.061	0.5–2.8	1.65

[a] The estimated precision of the perovskite phase is ±0.1%.

[b] The estimated precision of the density is ±0.1%.

[c] The estimated precision of the grain size is ±10%.

A35

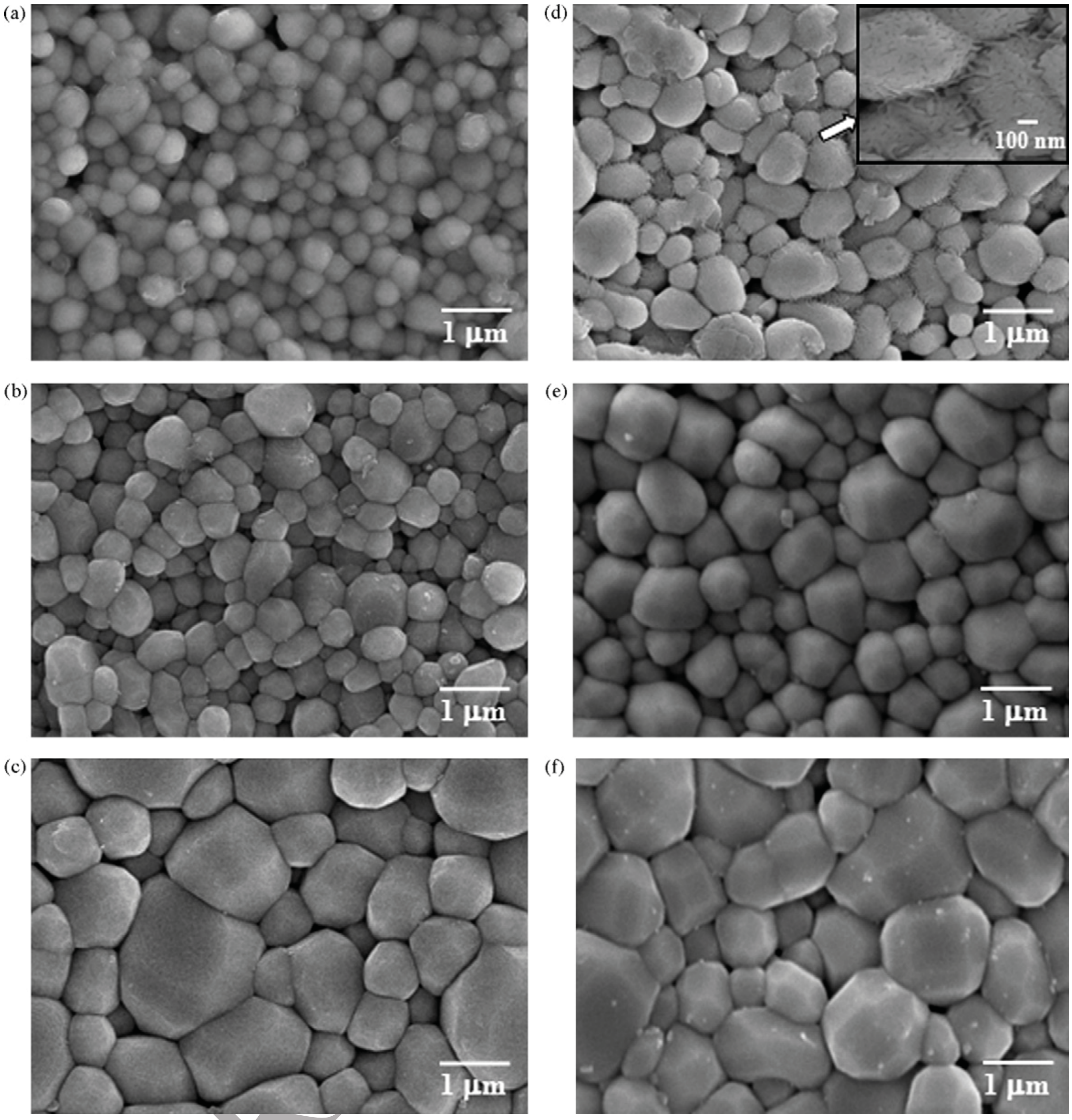

Fig. 3. Free surface of PT composites reinforced with PT nanopowders after sintered at (a) 1150 °C, (b) 1175 °C and (c) 1200 °C, and reinforced with PT nanofibers after sintered at (d) 1150 °C, (e) 1175 °C and (f) 1200 °C, for 2 h.

method of PT matrix reinforced with PT nanofibers was preferable for obtaining dense PT ceramics.

Interestingly, all the nanocomposite samples sintered at 1150–1200 °C remained unbroken. It may be assumed that the nanocomposites consisting of very fine dispersoids suffer less deformation, caused by the high value of c/a ratio, than the ceramics with significantly large grains (Table 1). Consequently, the experimental work carried out here suggests that the optimum conditions for forming the highly dense PT samples in this work are both types of PT/PT nanocomposites sintered at 1200 °C, 2 h dwell time, and 1 °C/min heating/cooling rates.

The dielectric properties of PT samples fabricated with different techniques are also compared in Table 2. In general, they all behave as typical normal ferroelectric materials [3]. The Curie temperatures are about the same for all samples measured whilst the variation of dielectric constant and dielectric loss of both types of PT nanocomposites seems to be somewhat related to the sintering temperatures. This observation indicates that densification and the presence of the second phases accompanied with porosities are the key factors responsible for the dielectric response of the products. Moreover, this study demonstrated that the dielectric properties of PT ceramics are also influenced by microstructural features and arrangement especially the microcracks and final density rather than by only grain size itself.

Table 2
Dielectric properties of PT ceramics derived from different fabrication techniques

Processing [Ref.]	Frequency (MHz)	T_C (°C)	$\varepsilon_{25°}$	$\varepsilon_{r,\max}$	$\tan\delta_{\max}$
Normal sintering [13]	1	482	243	7680	1.07
Two-stage sintering [20]	1	484	209	8198	0.95
Composite reinforced with nanopowders	1	486	244	8523	1.09
	3	486	245	7517	0.91
	5	487	247	7144	0.76
Composite reinforced with nanofibers	1	488	248	9104	0.81
	3	489	246	7110	0.57
	5	489	242	6801	0.45

A36

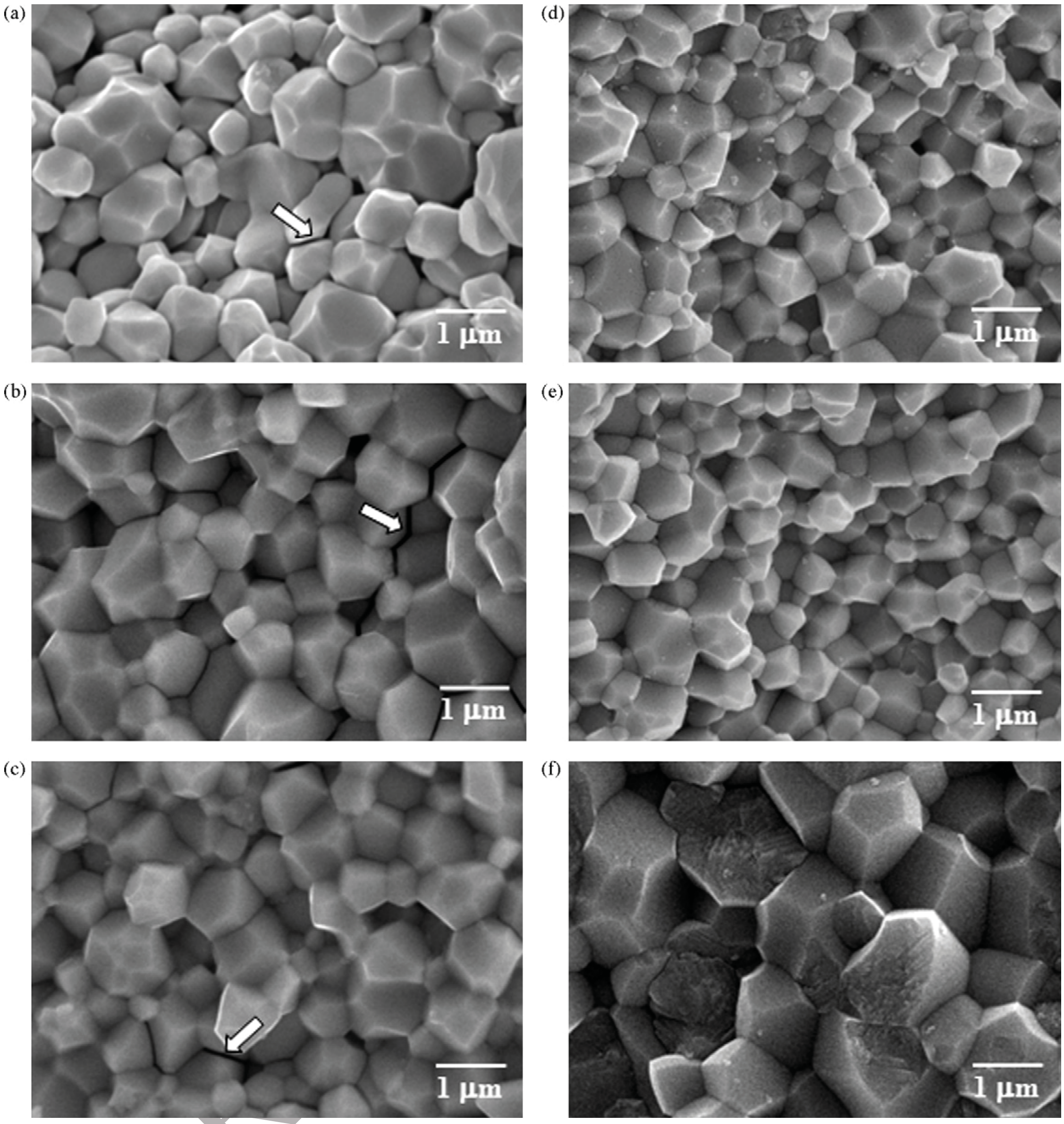

Fig. 4. Fracture surface of PT composites reinforced with PT nanopowders after sintered at (a) 1150 °C, (b) 1175 °C and (c) 1200 °C, and reinforced with PT nanofibers after sintered at (d) 1150 °C, (e) 1175 °C and (f) 1200 °C, for 2 h.

The different microstructure and the different amount of secondary phases present in the sintered PT ceramics strongly influence the dielectric properties of these materials, leading to relatively superior dielectric behavior in PT/PT nanocomposites. The secondary phases in conventional PT sample are interconnected at grain boundaries and, as suggested by Wang and Schulze [31], exert more influence on the dielectric properties than when they are isolated. The influence of densification and microcracks on dielectric properties of these PT composites can be clearly observed in Fig. 5, where the dielectric constant and dissipation factor as a function of temperature are shown, respectively.

The maximum dielectric constant values at 1 MHz in both PT nanocomposites were 2–5% higher than in two-stage sintering and conventional PT samples (Table 2). As mentioned earlier, the reason for this is the high amount of secondary phase present in conventional PT ceramics and the presence of a PbO-rich secondary phase, with low dielectric constant, which could form a continuous layer between grains, decreasing the dielectric constant of the two-stage sintering samples [13,36].

The results obtained in this work suggest that, in general, these PT/PT nanocomposites exhibit complex microstructures which are inherently heterogeneous. The heterogeneity is a result of variation in grain size and orientation; variation in chemical homogeneity; and the presence and distribution of additional minor phase, pores and (micro) cracks. These factors, which are strongly influenced by the sintering conditions, have an important effect on the dielectric properties of the materials and their reproducibility. However, these results suggest that better densification can be introduced into piezoceramics by fabricating ceramic-nanocomposites reinforced with piezoelectric nanodispersoids. Two aspects of this study are significant: (i) reductions in the maximum required sintering temperature (or the required prolong firing time) are possible as compared to the conventional (or the two-stage sintering) method and (ii) a framework has been established for developing self-reinforced piezoceramic-nanocomposite technique for better

A37

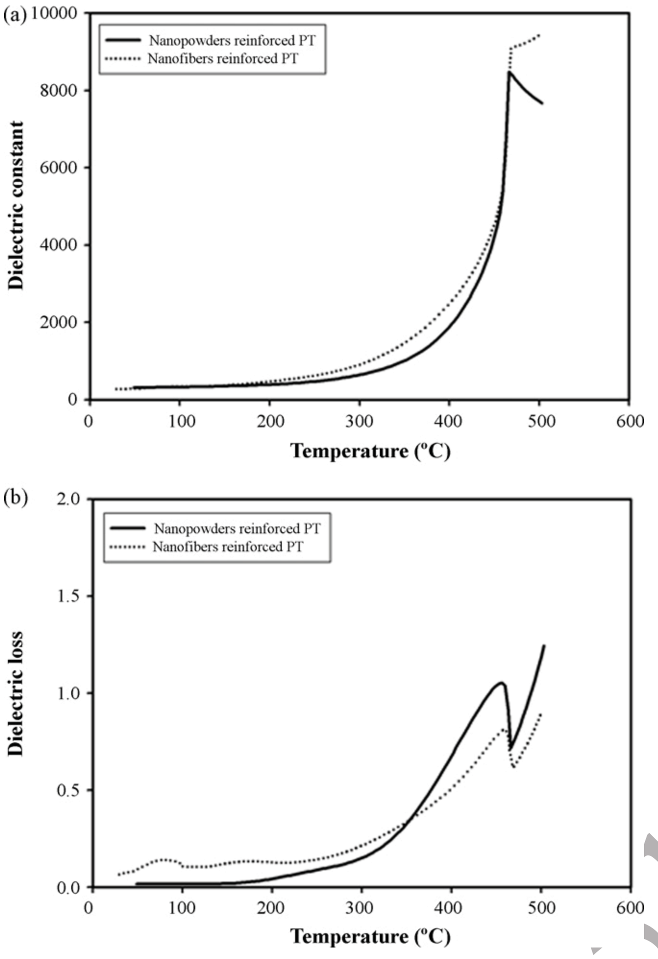

Fig. 5. Variation with temperature of (a) dielectric constant (ε_r) and (b) dielectric loss (tan δ) at 1 MHz for PT composites reinforced with PT nanopowders compared with those reinforced with PT nanofibers.

densification with retainable electrical properties of other piezoelectric materials, particularly those containing low melting point constituents.

For better understanding and verifying the attractiveness of the nanocomposite technique further, a systematic study on the effect of another piezoelectric nanodispersoids such as $BaTiO_3$ or PZT on the phase formation, densification, microstructure and electrical properties of the piezoelectric-based ceramic-nanocomposites is required.

4. Conclusions

The potentiality of a ceramic-nanocomposite technique as a low-cost and simple ceramic fabrication to obtain highly dense and pure PT/PT composites was demonstrated. It has been found that both densification and dielectric properties of the composites fabricated in this work were significantly enhanced, as compared to the two-stage sintering and the conventional PT ceramics, which is likely due to the fine-grain and reduced tetragonality as well as anisotropies of stress and domain motion in the composites.

Acknowledgements

We thank the Thailand Research Fund (TRF), the Commission on Higher Education (CHE) and the National Nanotechnology Center (NANOTEC), NSTDA, for all support.

References

[1] B. Jaffe, W.R. Cook, H. Jaffe, Piezoelectric Ceramics, Academic Press, New York, 1971.
[2] G.H. Haertling, J. Am. Ceram. Soc. 82 (1999) 797–818.
[3] A.J. Moulson, J.M. Herbert, Electroceramics, 2nd ed., Wiley, Chichester, 2003.
[4] T. Takahashi, Am. Ceram. Soc. Bull. 69 (1990) 691–695.
[5] L.E. Cross, Mater. Chem. Phys. 43 (1996) 108–115.
[6] G. Shirane, S. Hoshino, J. Phys. Soc. Jpn. 6 (1951) 265–270.
[7] G. Shirane, R. Pepinsky, B.C. Frazer, Acta Crystallogr. 9 (1956) 131–140.
[8] H. Takeuchi, S. Jyomura, E. Yamamoto, Y. Ito, J. Acoust. Soc. Am. 72 (1982) 1114–1120.
[9] L.B. Kong, W. Zhu, O.K. Tan, J. Mater. Sci. Lett. 19 (2000) 1963–1966.
[10] T. Suwannasiri, A. Safari, J. Am. Ceram. Soc. 76 (1993) 3155–3158.
[11] T. Takeuchi, M. Tabuchi, I. Kondoh, N. Tamari, H. Kageyama, J. Am. Ceram. Soc. 83 (2000) 541–544.
[12] J.S. Forrester, J.S. Zobec, D. Phelan, E.H. Kisi, J. Solid State Chem. 177 (2004) 3553–3559.
[13] A. Udomporn, K. Pengpat, S. Ananta, J. Eur. Ceram. Soc. 24 (2004) 185–188.
[14] F. Ye, L. Liu, J. Zhang, M. Iwasa, C.L. Su, Compos. Sci. Technol. 65 (2005) 2233–2239.
[15] R. Gadow, F. Kern, A. Killinger, Mater. Sci. Eng. B 148 (2008) 58–64.
[16] T. Ohji, Y.K. Jeong, Y.H. Choa, K. Niihara, J. Am. Ceram. Soc. 81 (1998) 1453–1460.
[17] H.T. Chung, D.S. Cheong, C.S. Kim, Mater. Lett. 59 (2005) 920–924.
[18] S. Jiansirisomboon, A. Watcharapasorn, Curr. Appl. Phys. 8 (2008) 48–52.
[19] H. Beltran, N. Maso, E. Cordoncillo, A.R. West, J. Electroceram. 18 (2007) 277–282.
[20] R. Wongmaneerung, R. Yimnirun, S. Ananta, Appl. Phys. A 86 (2007) 249–255.
[21] A. Udomporn, S. Ananta, Mater. Lett. 58 (2004) 1154–1159.
[22] R. Wongmaneerung, R. Yimnirun, S. Ananta, Mater. Lett. 60 (2006) 2666–2671.
[23] A. Rujiwatra, N. Thammajak, T. Sarakonsri, R. Wongmaneerung, S. Ananta, J. Crystal Growth 289 (2006) 224–230.
[24] H. Klug, L. Alexander, X-ray Diffraction Procedures for Polycrystalline and Amorphous Materials, 2nd ed., Wiley, New York, 1974.
[25] R.L. Fullman, Trans. AIME 197 (1953) 447–452.
[26] S.L. Swartz, T.R. Shrout, W.A. Schulze, L.E. Cross, J. Am. Ceram. Soc. 67 (1984) 311–315.
[27] JCPDS-ICDD Card no. 6-452, International Centre for Diffraction Data, Newtown Square, PA, 2000.
[28] J. Tartaj, C. Moure, L. Lascano, P. Durán, Mater. Res. Bull. 36 (2001) 2301–2310.
[29] M.L. Calzada, M. Alguero, L. Pardo, J. Sol–Gel Sci. Technol. 13 (1998) 837.
[30] S. Ananta, N.W. Thomas, J. Eur. Ceram. Soc. 19 (1999) 1873–1881.
[31] H.C. Wang, W.A. Schulze, J. Am. Ceram. Soc. 73 (1990) 825–832.
[32] Y. Matsuo, H. Sasaki, J. Am. Ceram. Soc. 49 (1966) 229–230.
[33] S.R. Dhage, Y.B. Khollam, H.S. Potdar, S.B. Deshpande, B.D. Sarwade, D.K. Date, Mater. Lett. 56 (2002) 564–570.
[34] S. Ananta, N.W. Thomas, J. Eur. Ceram. Soc. 19 (1999) 2917–2930.
[35] S. Chattopadhyay, P. Ayyub, V.R. Palkar, M. Multani, Phys. Rev. B 52 (1995) 13177–13179.
[36] M. Villegas, A.C. Caballero, M. Kosec, C. Moure, P. Duran, J.F. Fernandez, J. Mater. Res. 14 (1999) 891–897.